

2016

Development of electro-optic systems for self cleaning concentrated solar reflectors

<https://hdl.handle.net/2144/17072>

"Downloaded from OpenBU. Boston University's institutional repository."

BOSTON UNIVERSITY
COLLEGE OF ENGINEERING

Dissertation

**DEVELOPMENT OF ELECTRO-OPTIC SYSTEMS FOR
SELF CLEANING CONCENTRATED SOLAR
REFLECTORS**

by

JEREMY W. STARK

B.S., University of Arkansas at Little Rock, 2009
M.S., Boston University, 2012

Submitted in partial fulfillment of the
requirements for the degree of
Doctor of Philosophy

2016

© 2016 by
JEREMY W. STARK
All rights reserved

Approved by

First Reader

Malay K. Mazumder, PhD
Research Professor of Electrical and Computer Engineering
Research Professor of Materials Science and Engineering

Second Reader

Mark N. Horenstein, PhD
Professor of Electrical and Computer Engineering

Third Reader

Siddharth Ramachandran, PhD
Professor of Electrical and Computer Engineering
Professor of Materials Science and Engineering

Fourth Reader

Soumendra N. Basu, PhD
Professor and Associate Division Head of Materials Science and Engineering

Fifth Reader

Nitin R. Joglekar, PhD
Associate Professor of Operations and Technology Management
Deans Research Fellow

Sixth Reader

Julius E. Yellowhair, PhD
Senior Optical Systems Engineer
Sandia National Laboratories

Magnetic forces do no work.

David J. Griffiths, *Introduction to Electrodynamics*

Acknowledgments

I would like to thank my friends and family for their support during my academic career, including a special acknowledgment to my wife Jessica Jones for her patience and understanding of long hours spent in cleanrooms and testing labs. I would also like to acknowledge the support of undergraduate researchers who have worked in the Applied Electromagnetics lab in support of this work, and the other graduate students who have also worked in other aspects of this project. I am very grateful for the support of my advisors, Professor Malay Mazumder and Professor Mark Horenstein, who have supported me and provided valuable guidance over the duration of my undergraduate and graduate research. I would like to thank the rest of my committee for their support and feedback during the process of finishing my dissertation. This work has been supported through the US Department of Energy SunShot program grant number DOE DE-EE0005794, the Massachusetts Clean Energy Center (MassCEC) Catalyst Program, the Binational Science Foundation, The Arava Institute for Environmental Studies, Corning Inc., Abengoa Solar, MagCanica, and Sandia National Laboratory Solar Thermal Test Facility. I would also like to acknowledge Paul Mak and the Boston University Optoelectronic Processing Facility for training and maintaining the equipment necessary for this research.

DEVELOPMENT OF ELECTRO-OPTIC SYSTEMS FOR SELF CLEANING CONCENTRATED SOLAR REFLECTORS

JEREMY W. STARK

Boston University, College of Engineering, 2016

Major Professor: Malay K. Mazumder, PhD
Research Professor of Electrical and Computer
Engineering
Research Professor of Materials Science and
Engineering

ABSTRACT

The current demand for energy usage in the world is increasing at a rapid pace; in China alone, the electricity usage has increased by 12% per year from 2006-2010, where more than 75% of electrical power is produced by coal burning facilities (Mathews and Tan, 2013). Numerous studies have shown the effects of carbon dioxide emissions on global climate change, and even showing the permanence of high carbon dioxide levels after emissions cease (Solomon et al., 2009). Current trends away from carbon emitting power facilities are pushing solar energy into a position for many new solar power plants to be constructed. Terrestrial solar energy at AM1.5 is generally given at $1\text{kW}/\text{m}^2$, which is a vast free source of energy that can be harvested to meet the global demand for electricity (Morton, 2006). Aside from some areas receiving intermittent levels of solar insolation, one of the largest hindrances to large

scale solar power production is obscuration of sunlight on solar collectors caused by dust deposition. In areas with the highest average solar insolation, dust deposition is a major problem for maintaining a constant maximum power output. The southern Negev desert in Israel receives on average $17\text{g}/\text{m}^2$ per month in dust deposition on solar installations, which in turn causes losses of a third of the total power output of the installation (Offer and Goossens, 2001). In these areas, water is a scarce commodity, which can only be used to clean solar installations at a prohibitive cost.

To resolve this problem, a cost effective solution would be the application of electrodynamic screens (EDS), which can be implemented by embedding a set of parallel electrodes into the sun facing surface of solar collectors, including concentrating mirrors or photovoltaic (PV) modules, and applying a low frequency pulsed voltage to these electrodes. Three major contributions made in the course of this research in advancing (EDS) for self-cleaning solar mirrors are: (1) development of non-contact specular reflectometer for solar mirrors that allows measurement of reflectance loss as a function of dust deposition, (2) development of a dust deposition analyzer capable of measuring size distribution of deposited dust and provides mass concentration of dust on the surface of the mirror, and (3) optimization of electrode geometry of EDS film for minimizing optical reflection losses caused by the lamination of the film on the mirror surface while maintaining high reflection efficiency with high dust removal efficiency. The non-contact specular reflectometer and the dust deposition analyzer allowed experimental investigation of reflection losses as functions of surface mass concentration of dust on mirrors for validation of the optical model presented in this study.

Contents

1	Introduction	1
1.1	Electrodynamic dust removal	2
1.2	Overview of Work	7
2	Physical Properties of Desert Sands	10
2.1	Sand sample compositions	10
2.2	Sand particle size analysis	11
2.3	Dielectric discharge properties of sand samples	13
3	Electrostatic Charging of Sand from Electrodynamic Screen Activation	17
3.1	Electrostatic charging of sand samples on electrodynamic screens . . .	17
3.2	Charging of sand due to applied three phase voltage on electrodynamic screens	27
3.3	Effects of humidity on sand charging on electrodynamic screens . . .	33
4	Modeling Optical Power Losses	36
4.1	Modeling power losses due to dust loading	36
4.2	Reflection Losses Due to Electrodynamic Screen Integration into Solar Mirrors	40
5	Development of Non-Contact Specular Reflectometer	43
5.1	Introduction	43

5.2	Design of device	43
5.3	Experimental setup	48
5.4	Results and discussion	51
5.4.1	PEDOT:PSS Electrodes	52
5.4.2	Chrome Electrodes	53
5.4.3	Silver Nanowire Electrodes	57
6	Optimization of Electrodes and Materials for Specular Reflection and Dust Clearance	60
6.1	Optimizing specular reflection	60
6.2	Optimization parameters space	61
6.3	Specular reflection model using FRED ray tracing software	65
6.4	Electrostatic force modeling	69
6.5	Optimization parameters and evaluation	73
6.6	Laboratory Testing of Dust Removal Mirrors	79
7	Development of a Three Phase Low Frequency Power Supply	83
7.1	Previously designed power supplies	83
7.1.1	Challenges encountered with old design	84
7.1.2	Limitations with 1 kV design	85
7.2	Simplified 2 kV power supply design	86
8	Conclusion	90
8.1	Future Work	91
	References	92
	Curriculum Vitae	95

List of Tables

2.1	Sand composition	11
2.2	Sand charge decay averages	15
3.1	Triboelectric series for contact charging of materials, materials at the top of the table tend to charge positive while materials lower on the list charge negative. This charging can be effected by other environmental conditions such as humidity and other materials present.	24
4.1	Simulated specular reflection results with laboratory measured initial (clean) specular reflection. Electrode widths and spacings were modeled after the initially produced panels.	42
5.1	Table showing electrode width and spacings for photolithographic chrome panels, along with the specular reflection values for two different orientation of electrodes	56
6.1	Table of electrode geometry studied in the optimization testing.	63
6.2	Table of measured specular reflection values, percent clearance, and the adjusted clearance factor.	78
7.1	Table of specular reflection values for trial with failed power supply	85
7.2	Rise and fall times for 2 kV waveform at 5 Hz.	87

7.3 Table showing the results of a trial with the 2kV supply applied after 10 trials with a 1kV applied three-phase voltage. The final trial shows a large increase in specular reflection after applying the 2kV three phase voltage. 88

List of Figures

1.1	Plot of voltage versus time waveform for powering an electrodynamic dust removal system. Green, red, and blue plots represent the time at which voltage pulses are applied at the electrodes, in a three-phase, 5Hz waveform.	3
1.2	Drawing showing the relationship of an electrodynamic screen (EDS) module mounted with a borosilicate glass mirror. On the top layer, a transparent dielectric material such as Corning Willow glass, polyurethane, or mylar is used to encapsulate and protect the electrodes and aid in triboelectric charging of uncharged particles. Below this are the electrodes placed onto a borosilicate glass mirror substrate.	4
1.3	Image showing a transparent electrodynamic screen printed on Corning Willow Glass, a flexible dielectric material that has been tested with EDS modules. This material is abrasion resistant and highly transparent, allowing for durability and extremely high specular reflectivity.	5
1.4	CAD drafted image showing a 3-phase spiral electrode pattern which allows a 3-phase waveform with a single pass printing method and three electrical connections.	6

1.5	CAD drafted image showing a 3-phase design with two bus bars and independent electrode connections for a third phase. This design allows a single pass printing method for electrodes, but requires multiple connections to the electrodes of the third phase, using a dielectric barrier to separate the phases.	7
2.1	Microscope image of Arizona Road Dust sample	12
2.2	Particle size distribution of Arizona Road Dust as measured with optical images. Particles sizes are binned in 5 micron increments from 0 to 60 microns for this sample.	13
2.3	Optical image of Arabian desert sand sample, taken with a Nikon Eclipse LV150 microscope.	14
2.4	Optical image of Arabian desert sand sample, taken with a Nikon Eclipse LV150 microscope.	15
2.5	Experimental setup for sand corona charging experiments. In the center of the image a grounded, metallic weighing dish that contains the sand sample is placed below a corona discharge needle, which can be remotely powered and moved. An electrostatic voltmeter probe can be remotely moved in place to measure the charge decay of the sand. . .	16
3.1	CAD rendering of test chamber, showing the vibrating sieve for depositing sand and angled stand for changing the angle of the test panel. In charge testing, a Faraday cup would be placed under the test stand to collect charged sand.	19

3·2	Plot of sand charging for Dubai desert sand sample.	20
3·3	Plot of sand charging for Negev desert sand sample.	22
3·4	Dubai sand chaging for EDS while not activated, shaken, and activated	25
3·5	Charge to mass ratio for applied voltages with Dubai desert sand. . .	28
3·6	Graph showing the calculated percent saturation charge based on the mean particle diameter and the net charge measurement for 900 volt applied voltage tests.	30
3·7	Graph showing the calculated percent saturation charge based on the mean particle diameter and the net charge measurement for 950 volt applied voltage tests.	31
3·8	Graph showing the calculated percent saturation charge based on the mean particle diameter and the net charge measurement for 1000 volt applied voltage tests.	32
3·9	Plot of charge to mass measurements for Dubai sand at varying hu- midity levels	34
4·1	Dust deposition of JSC-1A Lunar regolith modeled on photovoltaic module along with predicted data based on particle size distribution .	37
4·2	Scattering plot calculated for 1 micron sand at 655 nanometer wave- length source.	38
4·3	Comparison of specular reflection values with calculated results. . . .	40

5.1	Image of a hand-held specular reflectometer, D& S model 15R, made by Devices and Services Company. The reflectometer is placed onto the surface that is to be tested, which can interfere with dust on the solar mirror that is being tested.	45
5.2	Rendering of the specular reflectometer, which shows the collimated LED source, testing surface, and receiving optics, with the optical angle between the source and receiver.	46
5.3	Initial calibration data for noncontact specular reflectometer, based around measurements from multiple mirrors with varying quality of specular reflection	49
5.4	Testing chamber for controlling environmental conditions and containing dust deposition for testing solar mirror specular reflection under dust loading conditions and self-cleaning performance of electrostatically enhanced mirrors.	50
5.5	Graph showing dust loading on a mirror with non-contact specular reflectometer taking measurements of reflection as JSC-1A Mars simulant test dust is used.	52
5.6	Graph showing dust removal performance of PEDOT:PSS electrodes taken with non-contact specular reflectometer over ten dust loading and cleaning cycles in an environmental chamber.	54
5.7	Graph showing dust removal performance of chrome electrodes taken with non-contact specular reflectometer over ten dust loading and cleaning cycles in an environmental chamber.	55

5.8	Graph showing dust removal performance of AG-NW electrodes taken with non-contact specular reflectometer over ten dust loading and cleaning cycles in an environmental chamber.	58
6.1	Plot of the optimization parameters. The electrodynamic screen parameters shown are the inter-electrode spacing on the y-axis, and the width of the electrodes on the x-axis. Each point on the plot represents a testing point in the study.	65
6.2	Image of the CAD model with ray tracing lines drawn from FRED Optical Engineering software, showing multiple reflections from the mirrored surface and embedded electrodes.	66
6.3	Plot of predicted specular reflection from the FRED ray tracing model is shown in the red line. The plot of the specular reflection measurements from the fabricated test panels is shown in the black points.	68
6.4	Plot of the forces acting on sand particles on an electrodynamic screen as a function of particle size. Force in newtons is shown on the y-axis, particle diameter in microns is shown on the x-axis. Forces plotted are the electrostatic image force as the dashed line, Coulomb force as the solid line, and Van der Waals force as the dotted line.	72
6.5	Plot of the ratio of adhesive and repulsive forces acting on sand particles on an electrodynamic screen as a function of particle size. The y-axis shows the ratio of forces, with a ratio over one being a net repulsive force. The x-axis shows the particle diameter in microns.	74

6.6	Image showing the Dust Deposition Analyzer, a device that scans the surface of a solar device and takes multiple images over the test surface. The instrument then uses MATLAB image processing toolbox to analyze the percentage of the surface area covered by dust particles. .	75
6.7	Images showing the clearance from a panel, using a dust particle imaging system to scan the surface and determine dust removal. The first image shows before dust deposition, the second image is after dust deposition, and the third is after EDS activation.	77
6.8	Plot showing the results of the clearance factor, which is a function of the initial specular reflection and the percent clearance of the panel. The line shows a 90 percent value of clearance and specular reflection.	79
6.9	Laboratory testing for dust removal mirror module with PEDOT:PSS electrode materials.	81
6.10	Laboratory testing for dust removal mirror module with chrome electrode materials.	82
7.1	Image of a second generation power supply design.	84

List of Abbreviations

CAD	Computer-Aided Design
DEP	Dielectrophoretic Force
EDS	Electrodynamic Screen
\mathbb{I}	the Imaginary plane
PEDOT:PSS	Poly(3,4-Ethylenedioxythiophene) Polystyrene Sulfonate
r	Radius
\mathbb{R}^2	the Real plane

Chapter 1

Introduction

The demand for sustainable energy sources to replace depleted and increasingly difficult to obtain fossil fuel sources is causing a spur of investment and research into solar energy. Currently new research going into solar cells is pushing efficiency higher, where single junction cells are reaching close to 30% efficiency and multi-junction cells have pushed past 40% efficiency(Green and Emery, 2012). To maximize the energy output of these highly efficient cells, they will need to be placed into areas with high solar insolation. These areas are located in desert and semi-arid climates where high levels of dust deposition are present. As dust deposition on solar cells increases, the amount of incident solar radiation reaching the cells decreases, and the power output drops dramatically.

To keep the solar collectors, such as photovoltaic modules and solar mirrors clean, both passive and active methods of dust control have been applied to minimize energy yield losses due to dust deposition. In some large scale installations, specialized water cleaning trucks are used to periodically wash mirrors and photovoltaic modules, often at a large cost. While this method is effective, it is not viable in most desert areas where water is a limited resource, as with the example of the Southwestern United States, where the region is under water restrictions due to an ongoing

drought (Chaudhry et al., 2015). Other active devices have been considered that use pressurized air to blow away dust, vibration to mechanically dislodge dust, and wiper systems to physically brush the surface have been used in small scale installations, but have proven not viable in large scale deployment. Passive methods such as surface texturing to lower particle adhesion, and chemical treatments to effect surface energy are being researched, but these cannot actively remove dust that is deposited after long periods of time.

These problems can be resolved by employing an electrostatic removal system that requires little power, no moving parts, and no water for cleaning. This work will describe the process of design and testing of a set of transparent conducting electrodes embedded into glass front covers of photovoltaic cells, solar mirrors, and concentrating lenses, the theory behind the processes, operation and implementation of the devices, and will show that the electrodynamic screen devices are viable methods of removing dust from solar installations in large scale projects.

1.1 Electrodynamic dust removal

Electrodynamic movement of particles has been shown to be a proven method of facilitating particle transport for a wide variety of small particles. This process requires no moving parts, but a set of stationary electrodes to create the non-uniform electrostatic field to move the particles (Mazumder et al., 2013). The geometry of the electrodes can be adjusted to change the electrostatic field and control the movement of the particles, whether it be to direct the particles in a specific direction, or generally repel them from a surface, or collect them in a specified area (Mazumder et al.,

2014).

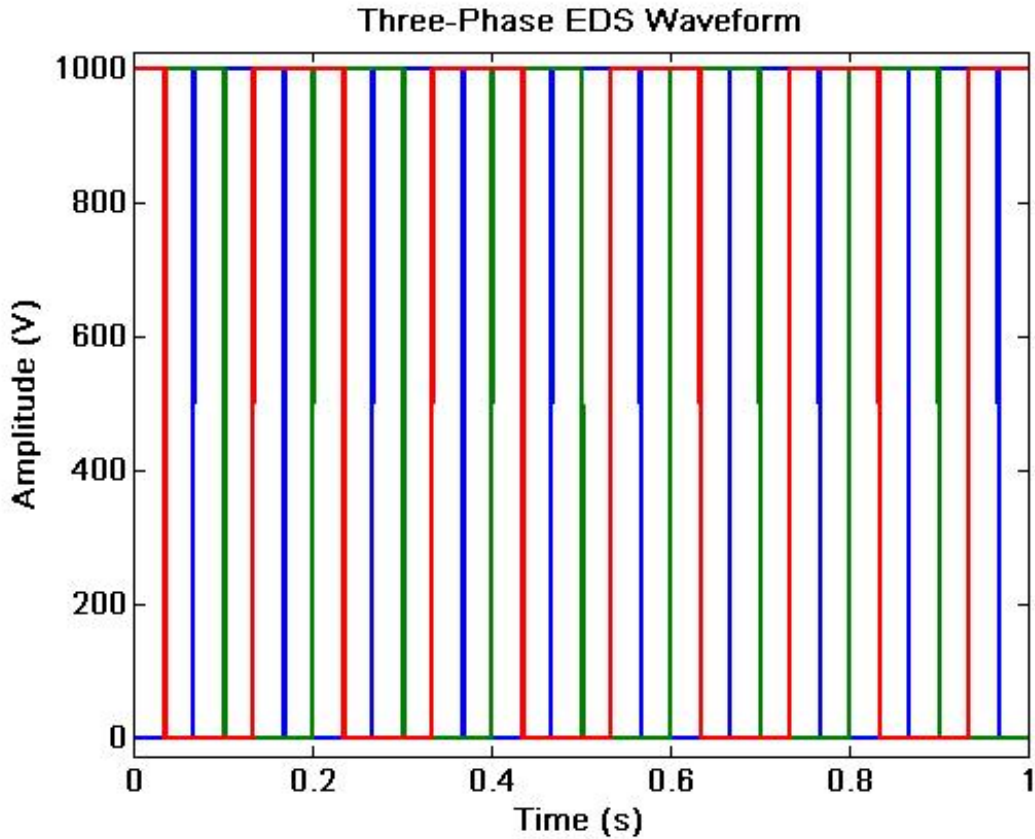


Figure 1-1: Plot of voltage versus time waveform for powering an electrodynamic dust removal system. Green, red, and blue plots represent the time at which voltage pulses are applied at the electrodes, in a three-phase, 5Hz waveform.

To form the traveling wave motion used to excite dust particles and move them from the surface, a three-phase pulsed voltage must be applied. Dust removal can be accomplished with a single phase motion, but the removal is not as efficient and can not direct particle motion (Mazumder et al., 2007). A plot of the three-phase pulsed voltage timing is shown in figure 1-1. In this figure the pulsed wave has a 50 % duty cycle, and a frequency of 5 Hz. Each phase is separated by 180 degrees.

The essential components to form an electrodynamic screen to remove dust from

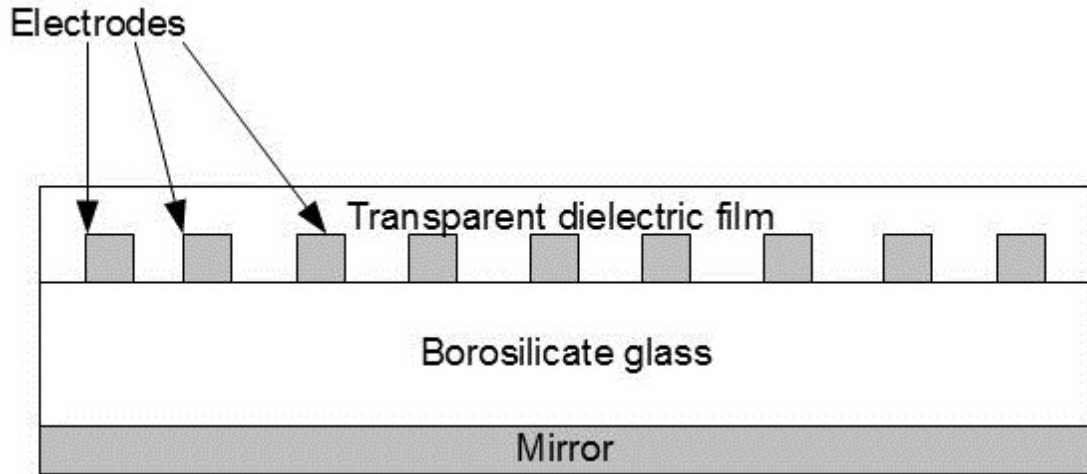


Figure 1-2: Drawing showing the relationship of an electrodynamic screen (EDS) module mounted with a borosilicate glass mirror. On the top layer, a transparent dielectric material such as Corning Willow glass, polyurethane, or mylar is used to encapsulate and protect the electrodes and aid in triboelectric charging of uncharged particles. Below this are the electrodes placed onto a borosilicate glass mirror substrate.

a solar mirror are: a borosilicate glass substrate with second surface mirrored reflector, transparent conducting electrodes, dielectric protective barrier covering the electrodes, and a three phase high voltage power supply. The power supply is discussed further in Chapter 7. The components of the mirror assembly are shown in figure 1-2, where the dielectric covering is shown as the top layer, the conducting electrodes are embedded in the dielectric barrier layer, and the borosilicate glass mirror assembly is below the electrodes.

The dielectric covering for the electrodes should be highly transparent, resistant to abrasion, provide enough electrical insulation for the applied voltage, and provide a material capable of triboelectric charging of sand particles. Polyurethane has been used and has provided a specular reflection above 90%, but is not stable enough for



Figure 1-3: Image showing a transparent electrodynamic screen printed on Corning Willow Glass, a flexible dielectric material that has been tested with EDS modules. This material is abrasion resistant and highly transparent, allowing for durability and extremely high specular reflectivity.

ultraviolet light or dust abrasion over long periods (Mazumder et al., 2014). Corning Willow Glass is highly transparent, UV stable, abrasion resistant, and flexible enough to be used on curved surfaces of parabolic trough solar reflectors. An image showing the flexibility of Corning Willow glass is shown in figure 1-3.

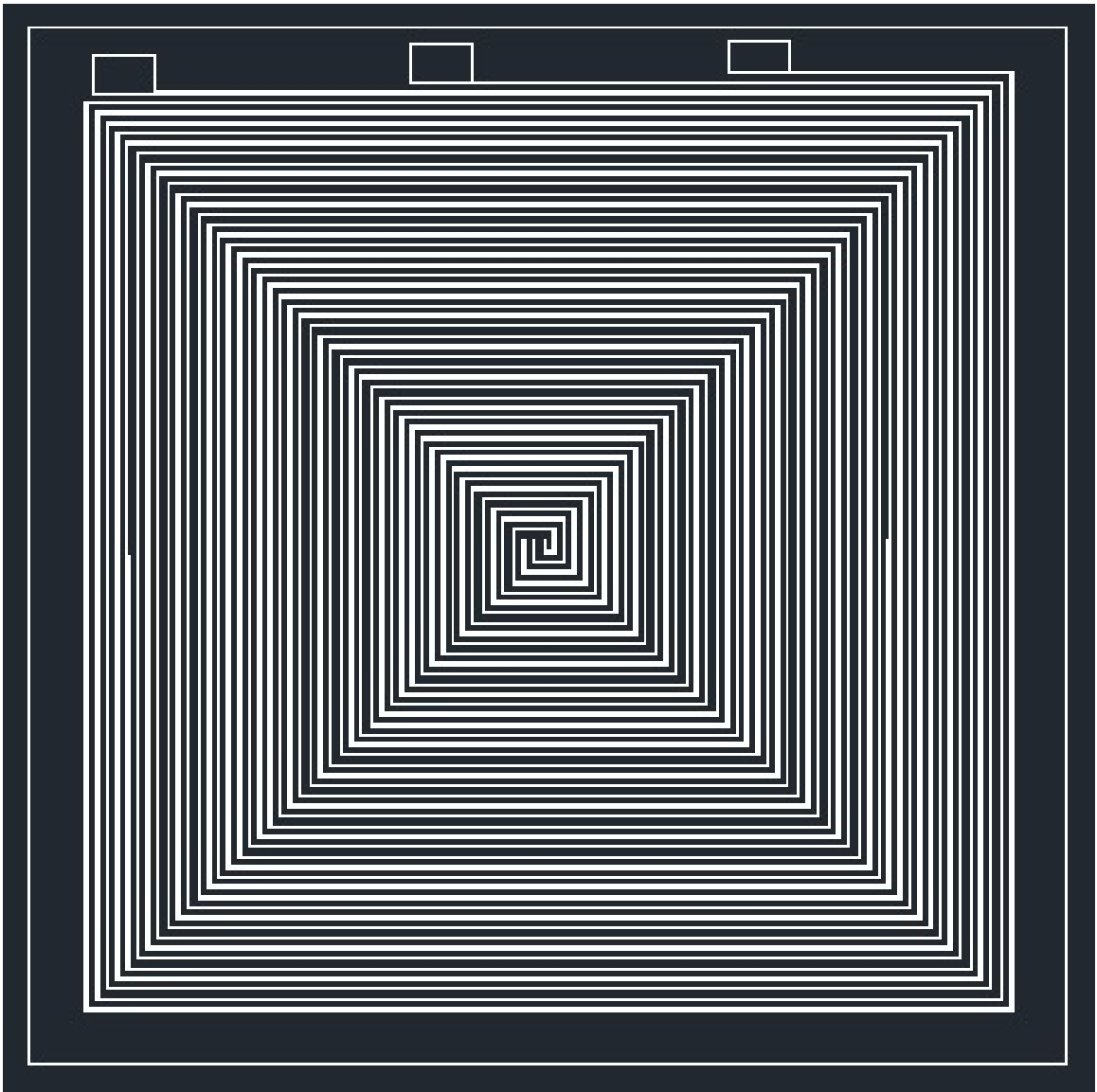


Figure 1-4: CAD drafted image showing a 3-phase spiral electrode pattern which allows a 3-phase waveform with a single pass printing method and three electrical connections.

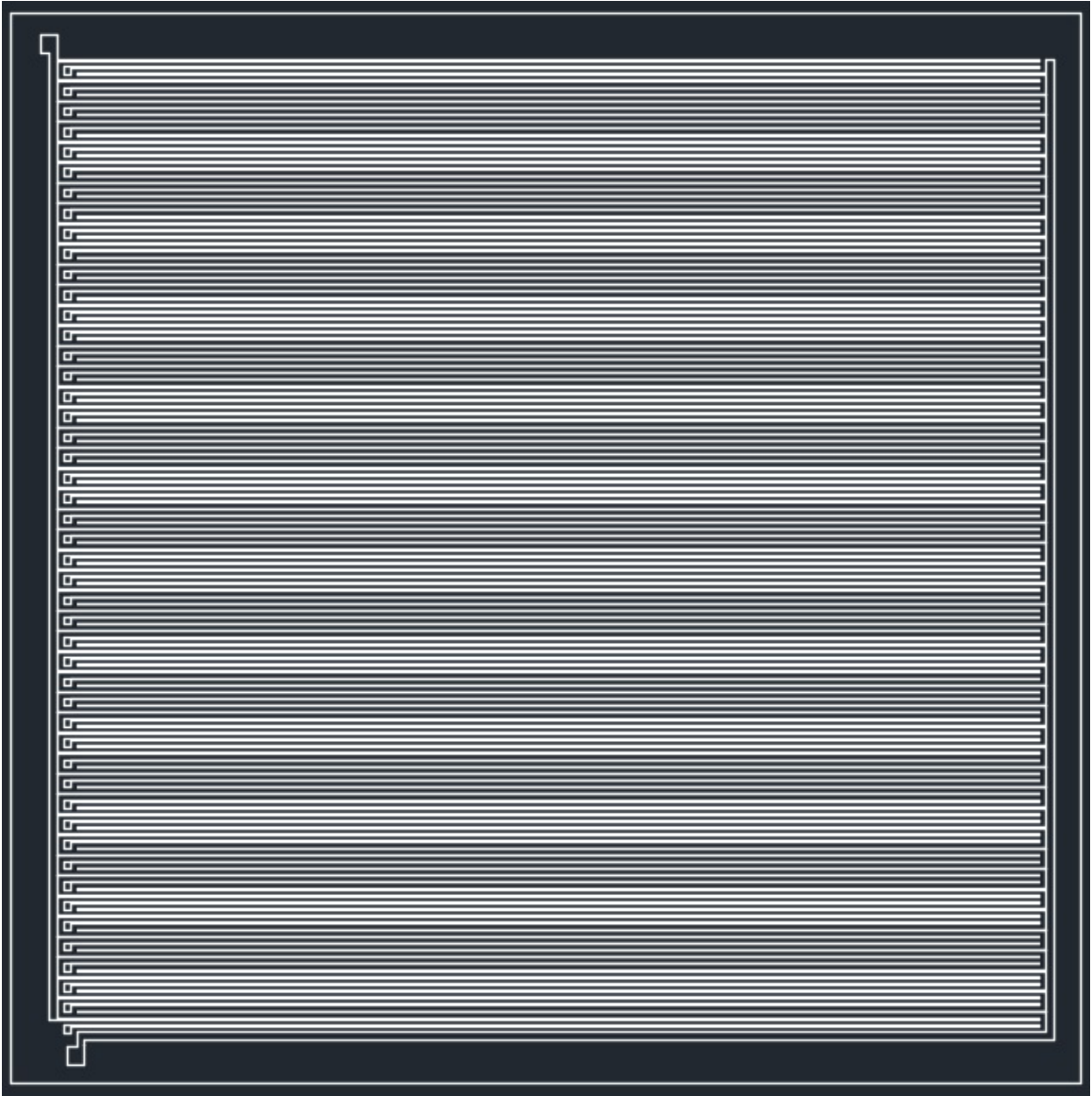


Figure 1.5: CAD drafted image showing a 3-phase design with two bus bars and independent electrode connections for a third phase. This design allows a single pass printing method for electrodes, but requires multiple connections to the electrodes of the third phase, using a dielectric barrier to separate the phases.

1.2 Overview of Work

To apply the principles of electrodynamic movement of particles to remove dust from solar mirrors, the basic concepts of dust removal will need to be evaluated, starting

with the optical and electrostatic properties of the sand that will be removed. The effect of the decrease of specular reflection on solar mirrors is shown in this work by modifying the Beer-Lambert law to consider a suspension of sand and Mie scattering compensation, coming to a predictable model of specular reflection degradation defined by sand particle size and dust deposition rates. The electrostatic properties of the sand requires a study of how the various types of sand will be effected by the applied electrostatic field and other forces present when in operation, and has been thoroughly evaluated in section 2.1.

The most important contribution to the study of dust removal technology that was developed through this work is the development of tools to measure and model specular reflection on mirrors in laboratory settings. Until this work, dust accumulation in solar reflectors has been studied in field installations, largely in regard to outdoor exposure in location specific studies (Pettit and Freese, 1980), (Goossens and Offer, 1995), (Offer and Goossens, 2001). By creating a generic model for specular reflection losses on solar mirrors that can be applied to multiple sand and dust types, predictive models for dust loading and cleaning can be developed for more efficient cleaning schedules for solar thermal installations. The model for specular reflection losses due to dust loading is discussed in Chapter 4. In addition to this modeling, the development of an instrument to measure real time specular reflection losses on reflection surfaces without interfering with the surface is a prime resource to allow dust removal to be studied and qualified in a laboratory scale. This instrument, a non-contact specular reflectometer is discussed in Chapter 5

The development and application of electrostatic dust removal on solar reflectors

is shown by the development of an optical ray tracing model, which was used to study the effect of the electrode geometry on the specular reflection of electrodes embedded in solar mirrors. Working from the results of the model, panels were fabricated using various methods and evaluated for dust removal performance and reflectivity. In this process, an instrument was made to allow for continuous non-interfering testing of specular reflectivity while soiling and cleaning mirrors.

A specialized power supply has also been designed for testing panels at voltages above 1 kilovolt, to study the effect of higher applied field strength on dust particle removal. Additionally, physical geometry of the electrodes and electrode interconnection were studied to allow for robust connection and testing during the development of the dust removal screens. The iterations of independent phase connections and multiple electrode connections are shown in 1-4, which allows for single connections to each electrode phase, and 1-5, which has single connections and busbar voltage distribution for two phases, and independent connections to the third phase of electrodes. Combining these aspects of study to develop self-cleaning solar mirrors is shown as functioning panels are evaluated in this work.

Chapter 2

Physical Properties of Desert Sands

2.1 Sand sample compositions

Dust accumulation in desert areas can average $17\text{g}/\text{m}^2$ per month, as shown in a study in the Negev desert. This amount of dust accumulation on a photovoltaic panel will relate to a drop of approximately 30% of total power output. In order to better understand and remove the dust accumulating on solar modules, modeling the process of dust deposition and removal becomes an integral part of studying this topic. Initially sand samples were collected from various locations around the world, along with manufactured simulant sand samples. Samples that were collected from environmental locations were baked at 300° Celsius for two days to dry the sample and remove any biological contaminants that might exist before testing. Samples were then sieved to remove any large particles or other contaminants before any laboratory testing.

The elemental composition of these samples was analyzed using a JEOL JSM-6100 scanning electron microscope with an energy dispersive spectrometer feature. The composition of each sample is shown in table 2.1. As shown in the table, all samples of sand that are being studied are silica based sands with various other trace materials.

Table 2.1: Sand composition

Sand	O	Si	Al	Fe	Ca	Mg	Na	K	Cl
AZ Road	50.4	36.5	4.5	3.0	1.8	NA	NA	2.4	NA
Dubai	45.3	14.2	1.6	5.0	7.7	5.8	7.3	NA	12.5
Negev	46.1	8.3	2.6	4.0	31.4	1.3	NA	1.4	1.2
Gobi 1	55.5	22.8	3.4	4.9	9.8	1.5	0.8	1.4	NA
Gobi 2	69.3	18.7	6.0	1.1	NA	2.2	1.0	NA	NA
Mojave	68.0	17.3	7.0	1.2	1.3	1.9	1.6	1.2	NA
Lunar	67.0	15.9	6.8	1.6	3.0	3.1	2.5	NA	NA
Mars	71.6	10.2	11.2	2.6	1.7	NA	NA	NA	NA
Singing	70.0	24.6	2.6	NA	NA	NA	NA	NA	NA

2.2 Sand particle size analysis

In addition to elemental analysis, the sand samples were analyzed for particle size distributions. Samples were deposited onto microscope slides using a vibrating sieve in an environmental chamber. The samples were then imaged using a Nikon Eclipse LV150 microscope with digital camera system. The images were processed offline using imaging software to detect particle edges and determine an average major diameter for particles.

Samples of sand varied in mean diameter from 5 microns for the Arizona Road Dust test sample, to 80 microns for the Gobi 1 desert sample. Manufactured samples like Arizona Road Dust, JSC-1A Mars, and Lunar regolith samples were compared against rated size ranges for accuracy of microscope measurements. The particle size distributions were recorded for later use in determining the optical and electrostatic

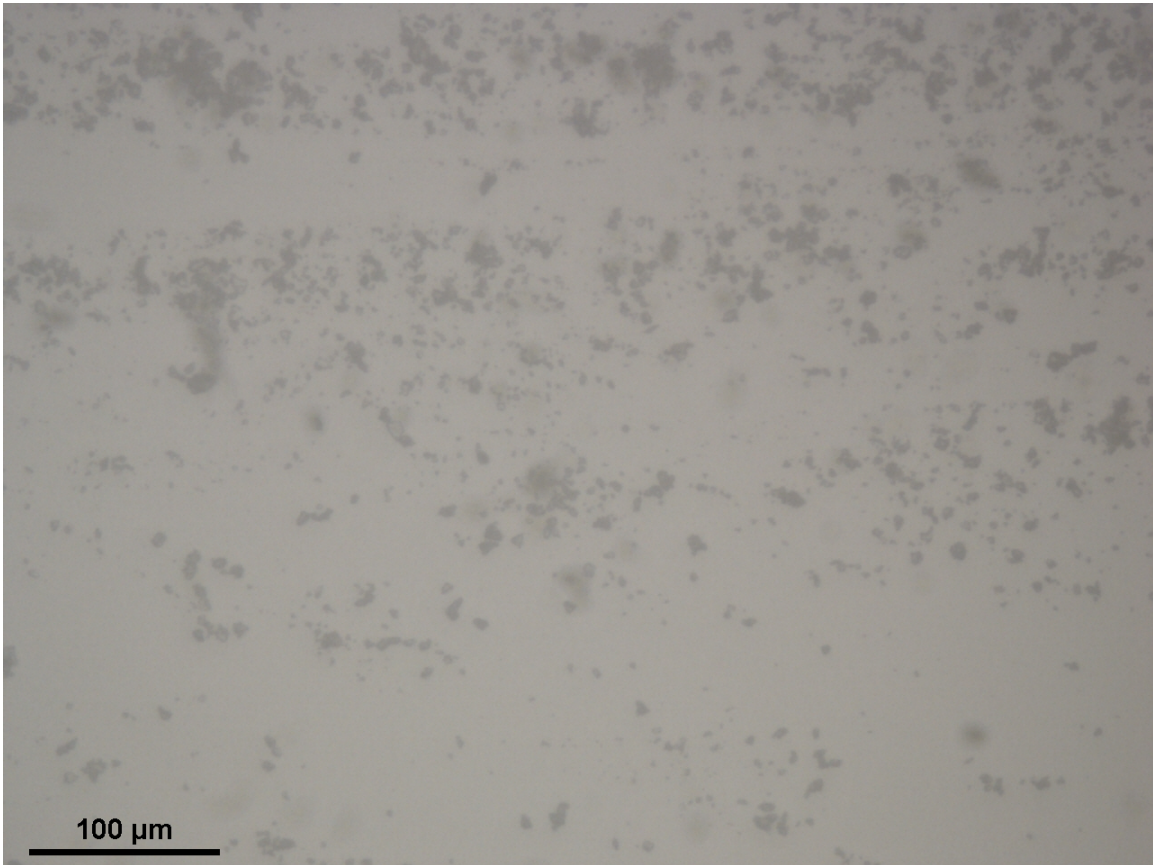


Figure 2-1: Microscope image of Arizona Road Dust sample

properties of the sand as it pertains to dust obscuration and removal on solar modules. The size distribution was normalized with particle volume, and calculated in 5 micron bins to reduce any random error from sampling. Due to limitations in the depth of focus of the microscope objective, some particles smaller than 1 micron could be underrepresented in the microscope imaging, but the smallest sample studied, Arizona Road Dust (ISO 12103-1 A1 Ultrafine), contains less than 10 percent of particles smaller than this range.

Optical analysis of non-manufactured sand samples has shown that a consistent uni-modal distribution was not present in all sand samples gathered from desert areas.

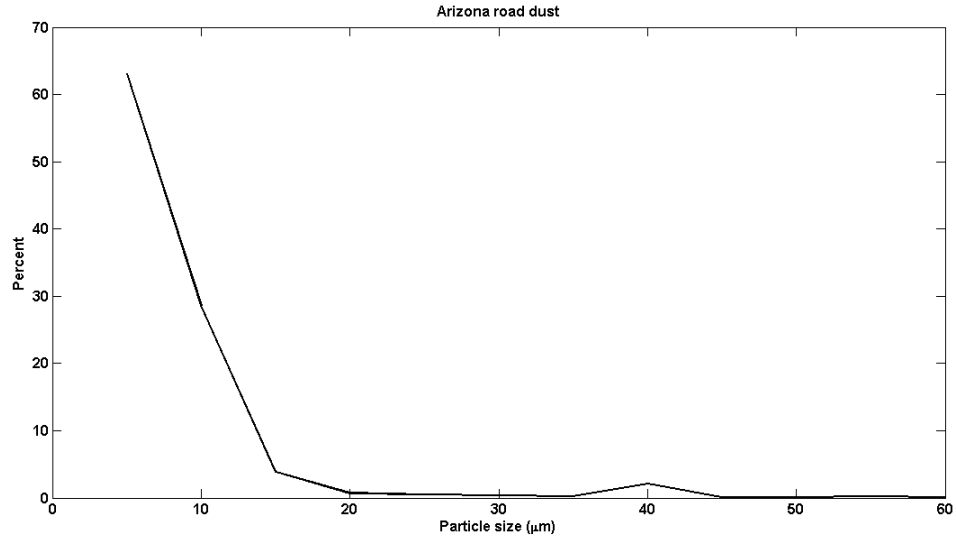


Figure 2-2: Particle size distribution of Arizona Road Dust as measured with optical images. Particles sizes are binned in 5 micron increments from 0 to 60 microns for this sample.

A microscope image of a desert sand sample from the Arabian desert near Dubai is shown in figure 2-3. The image shows a varied distribution of fine grains of sand along with larger grains. The particle size analysis of the optical image does have a bi-modal distribution, showing both large and small grain size particles are present in the sample. A plot of the particle size distribution of the Arabian sand sample is shown in figure 2-4. As shown in the plot, the distribution for the sand sample has peaks at both 10 microns and 60 microns.

2.3 Dielectric discharge properties of sand samples

After determining sand size ranges, to determine the varying dielectric properties of the sand samples, a charging experiment using a corona discharge and non contact electrostatic voltmeter was devised. The test used a corona needle with 4kV applied,

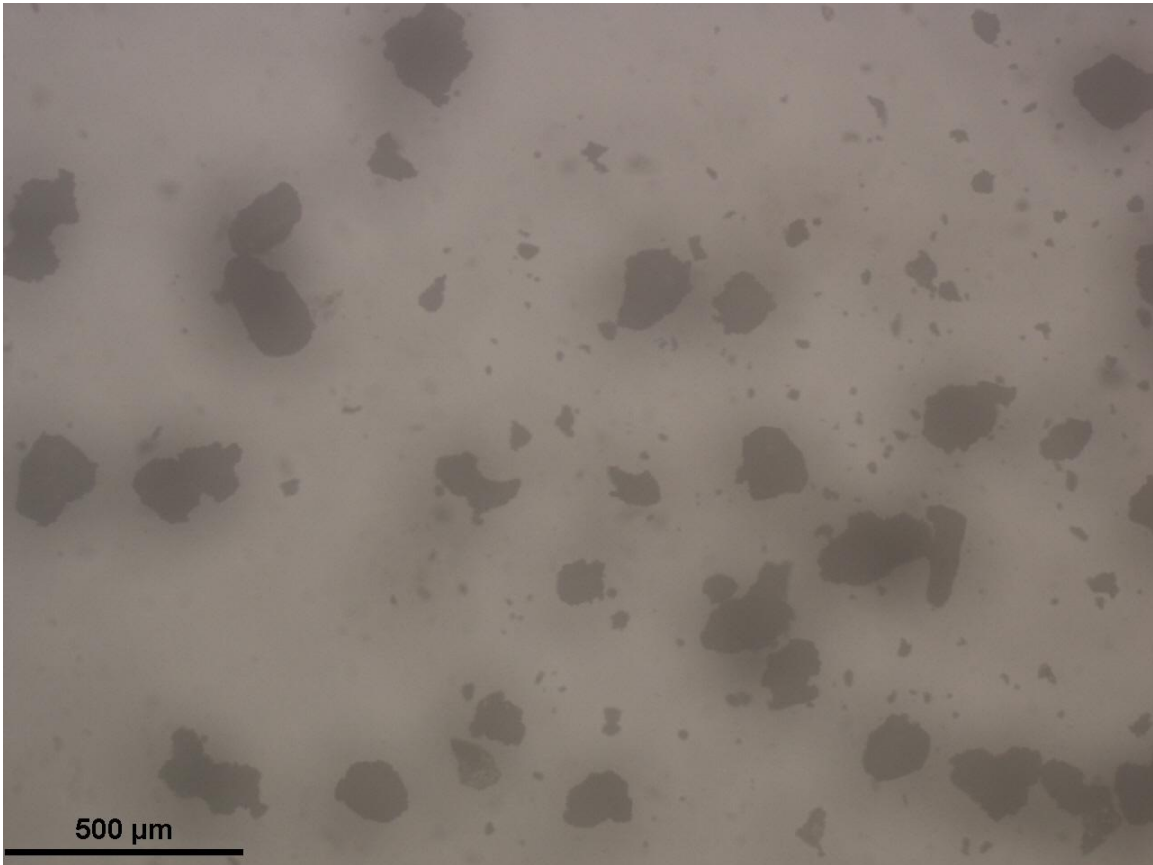


Figure 2-3: Optical image of Arabian desert sand sample, taken with a Nikon Eclipse LV150 microscope.

and a grounded aluminum weigh dish filled with a sand sample placed 1 inch below the corona needle. A sliding mechanism allows the corona needle to be moved from over the sample to the side, while simultaneously turning off the applied voltage and moving an electrostatic probe into place above the sand sample.

The electrostatic voltmeter is attached to a computer with Matlab via a Labview digitizer, and the decay of the potential is measured for each sand sample. The decay time of the sand varied in each sample from approximately 1 second in the Dubai sand sample to approximately 20 seconds in the JSC-1A Mars sample. The tests were repeated at controlled humidity of 15% RH and 40% RH. Table 2.2 shows the results

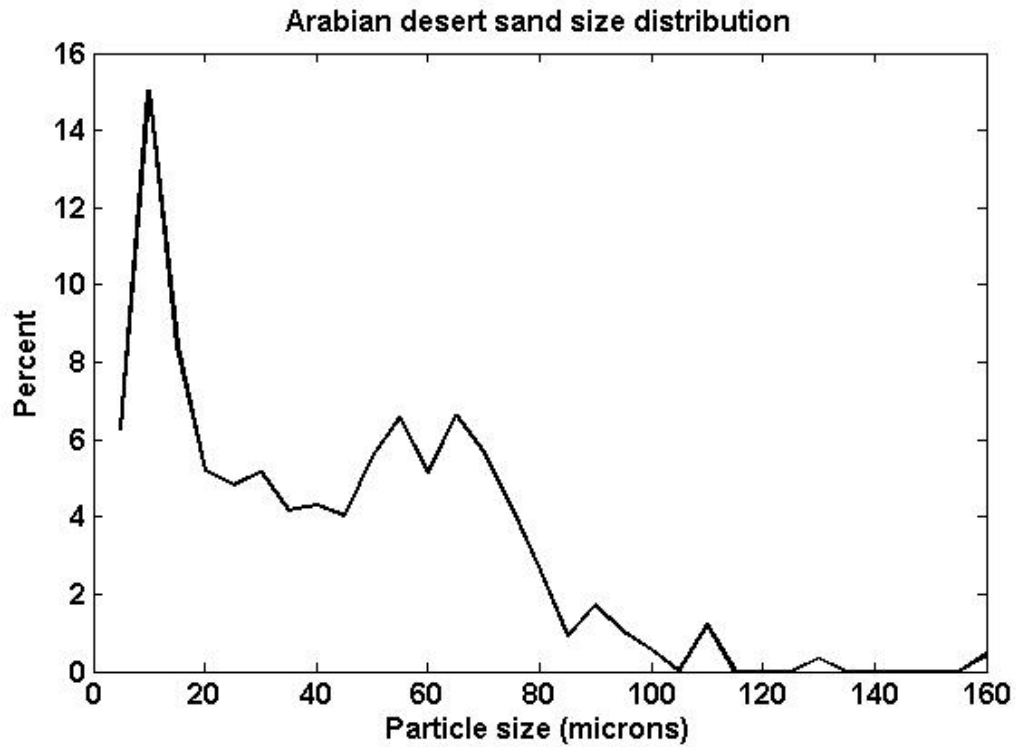


Figure 2-4: Optical image of Arabian desert sand sample, taken with a Nikon Eclipse LV150 microscope.

of the sand charging tests.

Table 2.2: Sand charge decay averages

	15% RH	40% RH
Dubai	1.457 sec	1.147 sec
Gobi	1.757 sec	1.090 sec
Lunar	4.469 sec	2.288 sec
Mars	17.984 sec	8.205 sec
Singing	5.664 sec	4.435 sec
Mojave	2.687 sec	1.842 sec

As expected, the charge decays at a faster rate at higher humidity, and the sands

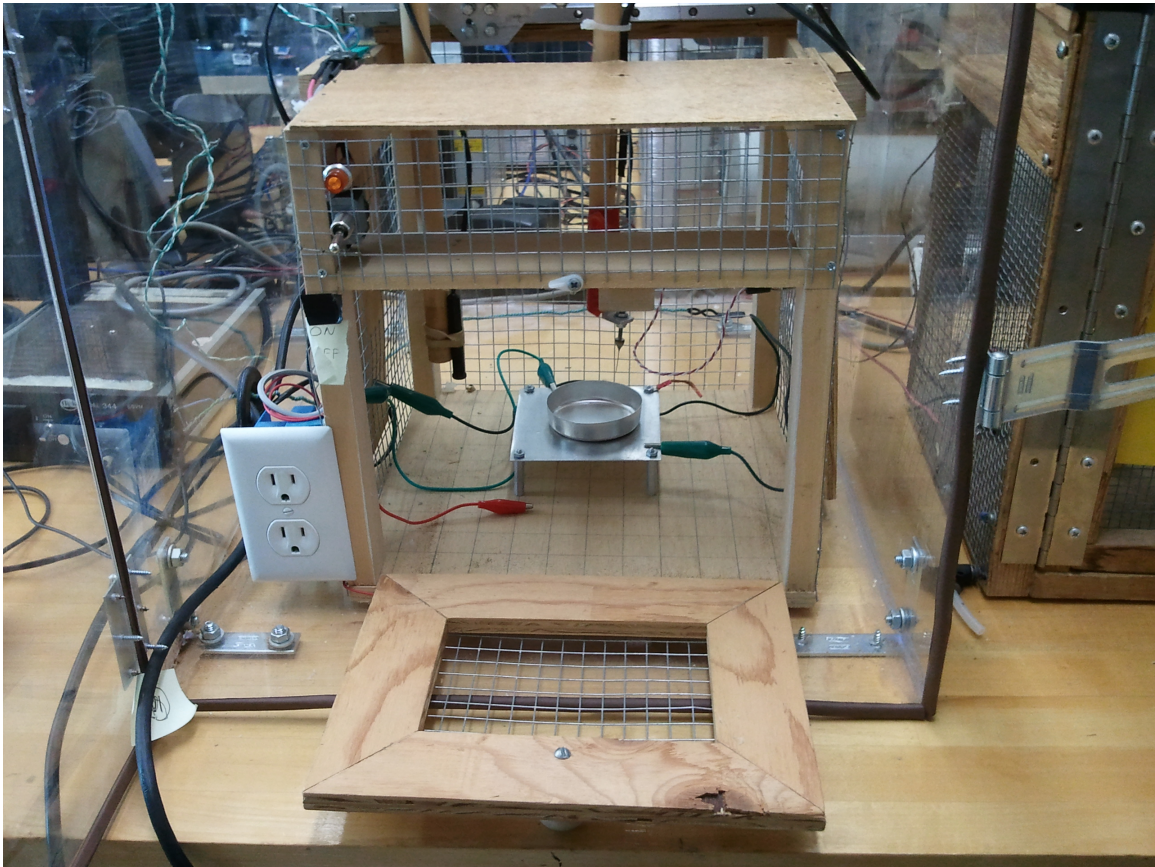


Figure 2-5: Experimental setup for sand corona charging experiments. In the center of the image a grounded, metallic weighing dish that contains the sand sample is placed below a corona discharge needle, which can be remotely powered and moved. An electrostatic voltmeter probe can be remotely moved in place to measure the charge decay of the sand.

with more iron composition decay faster than sand samples with less iron content. This information can be used to tailor electrostatic dust removal systems for areas with different composition of sands and different environmental concerns. For example, an area with higher relative humidity will experience less charge on sand particles, and will have to have a larger electrostatic field applied to remove sand.

Chapter 3

Electrostatic Charging of Sand from Electrodynamic Screen Activation

3.1 Electrostatic charging of sand samples on electrodynamic screens

A product of the process of dust removal from panels is the charging of sand particles. The sand itself is charged when an electric field is applied to the electrodes, causing dielectrophoretic forces, and then contact triboelectric charging of the of the particles on the surface of the electrodynamic screen. Initial investigation into the charging of sand for removal from solar panels was completed using printed circuit board models with the electrodes coated in commercial grade polyurethane film. The polyurethane film was 50 microns thick when coated with a Meyer rod, and 100 microns thick when using a spray coating method.

In various trials, sand was deposited onto the surface of the test boards with a vibrating sieve. The panels were placed on a 30 degree incline, as solar facing surfaces in the field would be at a similar angle, and the three phase high voltage waveform is applied to the electrodes. A Faraday cup is placed under the angled stand and attached to an electrometer to measure the net charge of the sand particles removed from the surface of the test panel after activation. The test setup is shown in figure 3-1,

with the vibrating sieve hanging from the top of the chamber, the test stand centered in the middle of the chamber, and environmental controls around the bottom of the chamber. The test stand is placed on a stand which connects to a balance below the chamber, which can determine the change in mass of the test panel. The Faraday cup that is placed below the edge of the test panel has a removable aluminum cup. This allows the sand that has been removed from the panel by the activation of the three phase high voltage wave form to be removed and placed on a balance to determine mass of the sample. Using the mass reading from the removed sand and the net charge measurement from the electrometer, the net charge to mass ratio of the removed sand can be determined.

Different sand samples were tested using the same printed circuit board test panels with electrodes coated with a 50 micron thick layer of polyurethane. The test samples of sand were prepared by sieving large particles (over 300 microns) and baking the sand for 24 hours at 300 degrees Celsius. The humidity was kept at 50 percent RH, and the temperature was 21 degrees Celsius. The first sample tested was a sample of sand from a desert in Dubai, which has a mean diameter of approximately 50 microns. The sand sample also has the highest iron concentration of all the samples tested at 5 percent by elemental composition as measured through energy dispersive spectroscopy using a scanning electron microscope. The composition of the sand sample is shown in table 2.1, in the second row. This sample of sand also had one of the lowest charge decay times after being charged with a corona charging device, as shown in table 2.2. The charge on this sample had decayed in just over one second at 40 percent relative humidity, and just under 1.5 seconds at 15 percent relative humidity.

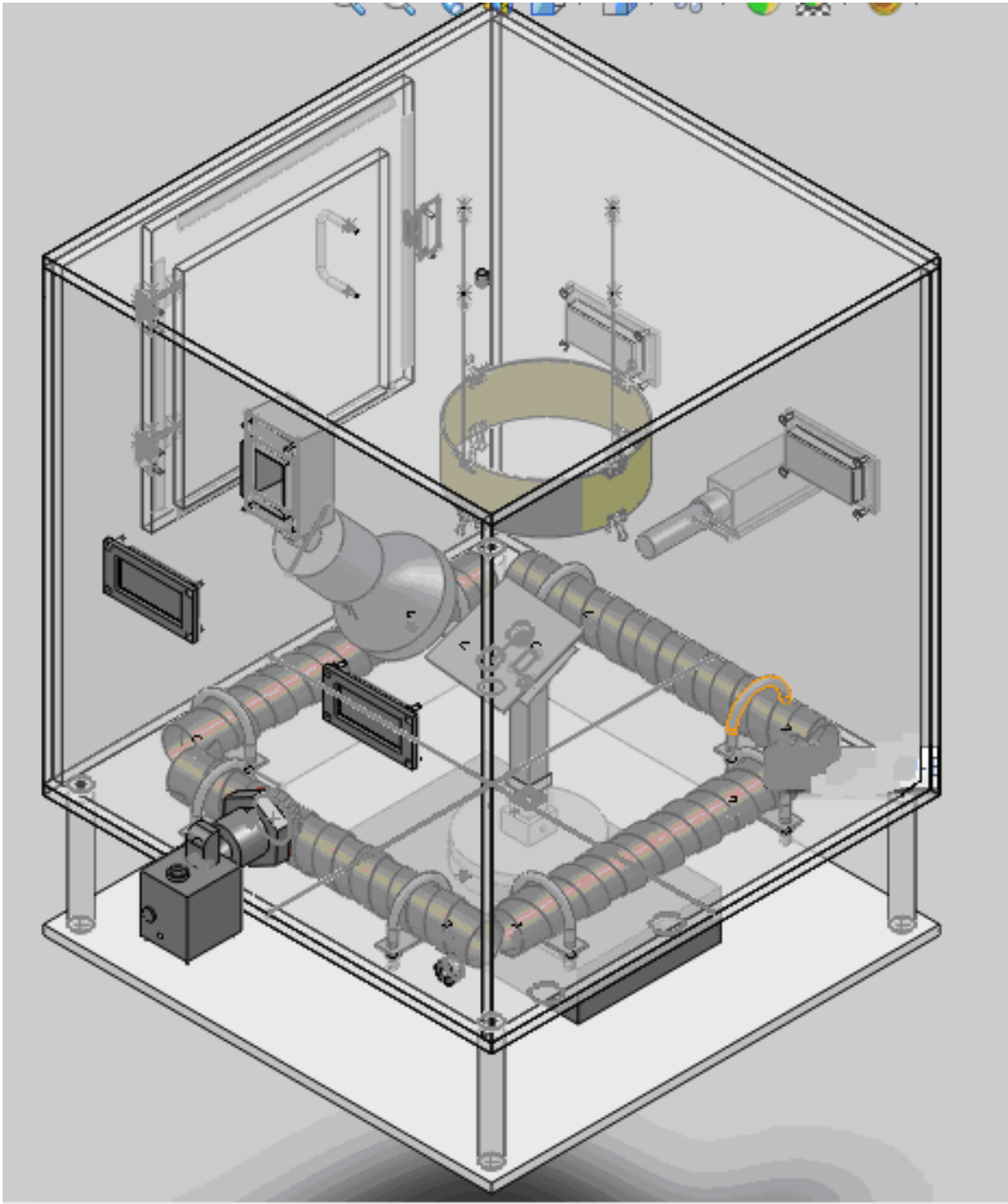


Figure 3-1: CAD rendering of test chamber, showing the vibrating sieve for depositing sand and angled stand for changing the angle of the test panel. In charge testing, a Faraday cup would be placed under the test stand to collect charged sand.

The first charge measurement was taken by activating the vibrating sieve and depositing dust directly into the Faraday cup, recording the net charge and the mass of the deposited sand. The result of this was a very small negative net charge to mass ratio, as shown in figure 3-2, in the blue bars of the bar graph. The small net negative charge is likely due to the metal mesh from the sieve, and the vibration motion to deposit the sand onto the test surface.

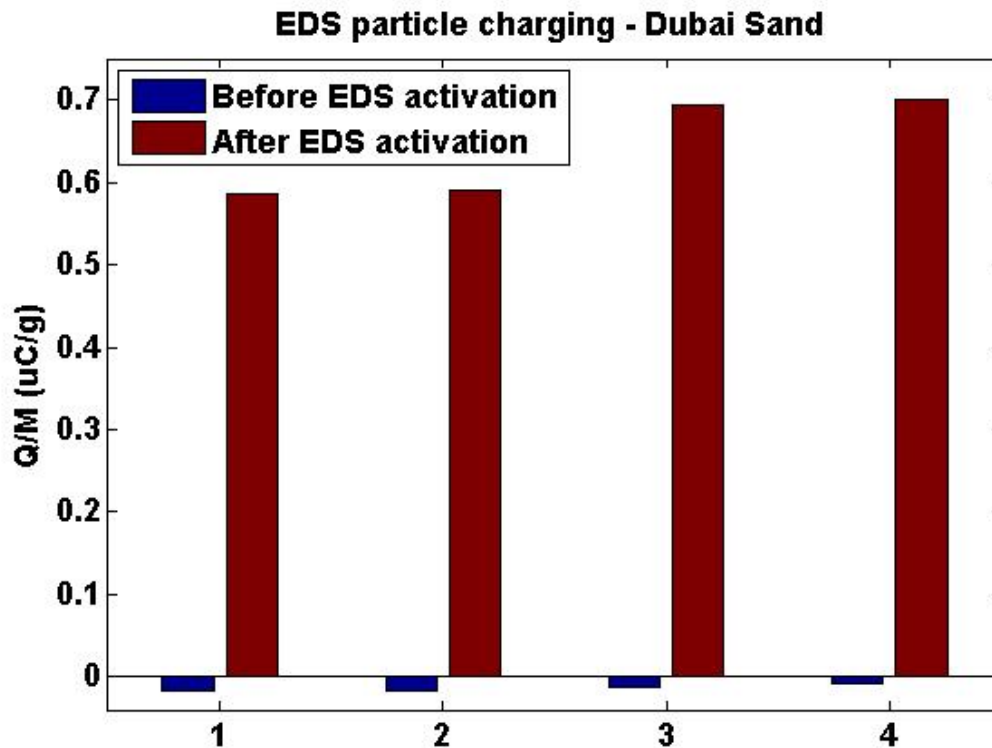


Figure 3-2: Plot of sand charging for Dubai desert sand sample.

After the initial charge of the deposited sand was determined, sand was deposited onto the surface of the test panel with the same conditions. After the deposition of the sand, the electrodes were activated with a three phase, 1 kilovolt waveform for one minute. The Faraday cup was placed under the test stand, and the net charge

was noted on the electrometer. The aluminum Faraday cup insert was removed and massed, and the charge to mass ratio for the test was calculated. The blue bars in the graph of figure 3.2 shows the net charge to mass ratio for a sample of Dubai sand. This shows a very large change in charge to mass ratio of the particles after activation of the EDS electrodes. The change in charge to mass ratio after EDS activation shows that a charging process is occurring which causes the net charge of removed particles to become several orders of magnitude larger, and charged in the opposite polarity of the initial sand that is deposited.

The test was repeated for a sand sample from the Negev desert in southern Israel. The sample was prepared in the same manner as the previous test, sieved with a 300 micron sieve and baked in an oven for 24 hours at 300 degrees Celsius. The sand sample has a mean particle diameter of 20 microns, which is smaller than the Dubai sand sample in shown in figure 3.2. The Negev sand sample also has a high concentration of calcium, as shown in the table 2.1, with 31.4 percent elemental composition, which is much less than the previously tested Dubai sample. The sand was first deposited into the vibrating sieve, which was activated and the sand was allowed to fall directly into the Faraday cup, where the net charge was noted on the electrometer. The aluminum insert was removed and massed using a balance, and the net charge to mass ratio was calculated for the sand as it was leaving the sieve. This value is shown in figure 3.3 as the blue bars in the bar graph. This shows a very small net positive charge to mass ratio, very similar to the Dubai desert sand sample shown in figure 3.2.

The Negev sand sample was then deposited onto a test panel using the vibrating

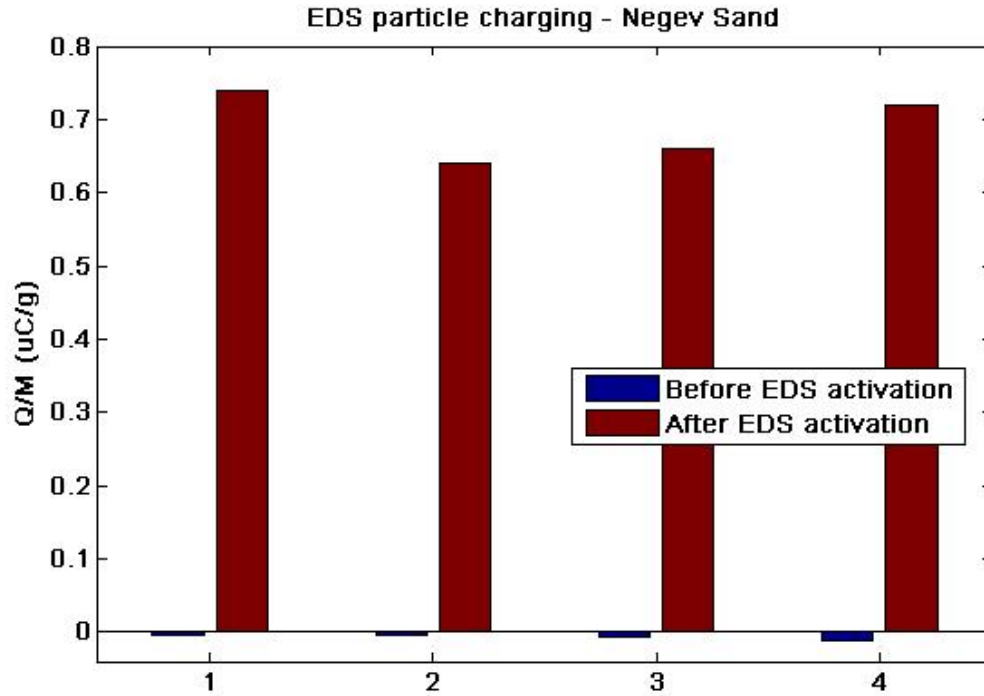


Figure 3-3: Plot of sand charging for Negev desert sand sample.

sieve, and the test panel was activated with three phase, 1 kilovolt waveform. The Faraday cup was again placed under the test panel to collect the charged sand as it was removed from the panel. The aluminum insert was removed from the Faraday cup after the test and the mass was recorded on a balance. The net charge to mass ratio was calculated, and is shown in figure 3-3 in the blue bars of the bar graph. The net charge to mass ratio is approximately the same as in the previous test with the Dubai sand sample. In both tests, it is shown that there is initially a very small net negative charge on the sand before deposition onto the panel. After activation with the three phase high voltage wave form, the sand becomes highly negatively charged when it is removed from the test surface and collected in the Faraday cup.

In both the Negev sand sample and the Dubai sand sample the charge to mass

ratio after the activation of the high voltage electrodes shows a large positive increase in net charge to mass ratio. From the triboelectric series, it is shown that silica glass is located on the far end of the positive triboelectric series as shown in table 3.1 (Moore, 1973). This shows that when a material that is more negative on the triboelectric series, the silica material should charge positively. The test panels were coated in polyurethane, which is shown to be on the negative side of the triboelectric series. As the sand is deposited onto the test surface which is coated in polyurethane, the sand particles will experience contact charging with the polyurethane coated surface. From the triboelectric series, the sand particles which are mostly composed of silica, will gain a positive net charge and the polyurethane coating will gain a negative net charge through the contact charging of the surface.

When the two materials come into contact, the charging of the sand particles is not instantaneous, and does require the repeated contact and separation of the sand particles and the polyurethane coating on the test surface. While the sand particles are being removed from the surface of the test panel, the sand particles will also come into contact with each other, causing charge exchange between the polyurethane surface and sand particles, and sand particles with other sand particles. Along with this charge exchange, the test panel electrodes create a strong non-uniform electric field along the surface of the panel, where the sand particles are interacting with the polyurethane coating.

To show the effect of the non-uniform electric field that is present when the test panels are activated, the sand must be subjected to a similar contact charging mecha-

Table 3.1: Triboelectric series for contact charging of materials, materials at the top of the table tend to charge positive while materials lower on the list charge negative. This charging can be effected by other environmental conditions such as humidity and other materials present.

Positive
Rabbit's fur
Cellulose acetate
Glass
Quartz
Mica
Wool
Cat's fur
Silk
Cotton
Wood
Amber
Resins
Metals
Polyurethane
Polystyrene
Polyethelene
Teflon
Cellulose Nitrate
Negative

nism with the polyurethane test surface as when the electric field is applied. This can be achieved by using a mechanism to shake the particles along the test panel surface, causing the sand particles to contact the polyurethane surface and the other particles of sand. Sand from the Dubai desert sample have been deposited onto the surface of a test panel, as in previous experiments. The sand sample was initially deposited into the Faraday cup directly to measure the initial charge to mass ratio of the sand as it is deposited from the vibrating sieve. After the sand was deposited, the charge was noted on the electrometer, and the mass of the Faraday cup insert was noted to determine the charge to mass of the sample. As with previous experiments, the charge to mass ratio of the sand sample deposited directly from the sieve was shown

to be a very small negative net charge to mass ratio.

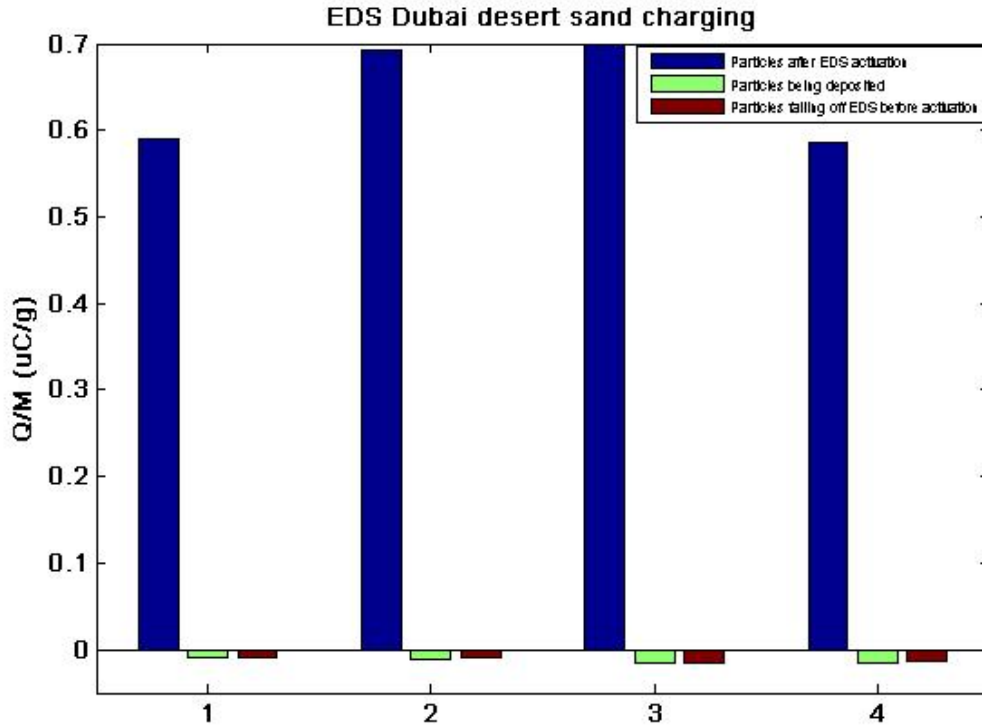


Figure 3-4: Dubai sand charging for EDS while not activated, shaken, and activated

After the initial charge of the deposited sand was determined, the sand was deposited onto the surface of the test panel. This time, instead of applying the three phase voltage to the electrodes, a vibration motor was activated on the panel, which caused the sand on the surface to move across the polyurethane coated test surface. The sand that was removed from the test surface was again collected in the Faraday cup, and the charge measurement was noted from the electrometer. The Faraday cup insert was removed and placed on a balance and the change in mass was recorded. The charge to mass of the sample was calculated and is shown in figure 3-4 as the red bar in the bar graph. In each trial the observed charge to mass of the sand that was

vibrated off of the surface of the test panel was shown to be a very small negative charge, but less than the charge to mass ratio of the sand as it initially leaves the vibrating sieve.

After the charge to mass of the sand interacting with the surface is measured without the application of the non-uniform electrostatic field, the sand is again deposited onto the surface of the test panel again. This time the three phase high voltage is applied to the electrodes and the sand is allowed to fall into the Faraday cup from the test panel. The charge is recorded from the electrometer connected to the Faraday cup, and the metal Faraday cup insert is removed and the change in mass is recorded. The charge to mass ratio is calculated, and shown in the graph in figure 3-4 as the blue bar in the bar graph. The charge to mass of the sand after activation again shows a very large net positive charge to mass ratio as in the previous trials.

This shows the charging of the sand particles experiences a greater change in charge when the three phase voltage is applied to the electrodes and the non-uniform electric field is created. When in this field the particles experience dielectrophoretic force due to the applied non-uniform field, which will cause rotational motion on the sand particles on the surface of the test panel. When there is no applied voltage causing the non-uniform electric field, the particles will not experience the same rotational motion. Instead, the vibration will cause more bouncing and sliding from the surface, leading to the difference of magnitude of change in the net charge to mass ratio of the sand collected in the Faraday cup. The electric field created by the applied voltage on the electrodes not only causes the particles to be repelled from the surface, but aides in charging the sand particles by creating a rotational motion

through a dielectrophoretic force. This motion initiates a charging process in the sand particles, where the sand particles become polarized and begin to experience a rotational force, and gather charge by a contacting polyurethane coating on the surface of the test panel.

3.2 Charging of sand due to applied three phase voltage on electrodynamic screens

Since the applied voltage contributes directly to the non-uniform electrostatic field, this could have an effect on the net charge of the particles removed from the surface of the testing panel. The power supply used for these experiments can vary the output voltage applied to the panel from about 200 volts to 1000 volts. The trial was repeated again, with the Dubai sand sample placed into the vibrating sieve, the humidity and temperature were controlled at 30 percent relative humidity and the temperature at 22.5 degrees Celsius. The test panel was again inclined at 30 degrees to the horizontal, and the Faraday cup with metal insert was placed under the edge of the panel. After the test panel was set up in the environmental chamber, the dust sample was deposited onto the test panel by activating the vibration motors on the sieve. The test panel was activated by applying the three phase 900 volt waveform to the electrodes. After activation the dust that fell from the surface of the test panel was collected in the Faraday cup, the charge from the electrometer was noted, and the change in mass of the Faraday cup insert was measured using a balance.

The charge to mass for the application of the 900 volt, three phase waveform was calculated, and shown in figure 3-5 as the blue bar in the bar graph. In this

trial, the charge to mass ratio for the sand that is removed from the surface of the of the test panel is highly positively charged, similarly to the previous tests. The trial was conducted for voltages of 700, 750, 800, and 850 volts, but this did not produce enough motion of the deposited sand sample to register a significant mass reading in the Faraday cup insert, and were discarded. The test was repeated with the same conditions for a 950 volt, three phase square wave signal. The results for this trial is shown in figure 3-5 as the green bar in the bar graph. The results of the test show similar readings of charge to mass ratio as the previous trial. The test was again repeated for 1000 volt three phase square wave signal applied to the test panel electrodes, and the results are shown as the red bar in the bar graph of figure 3-5.

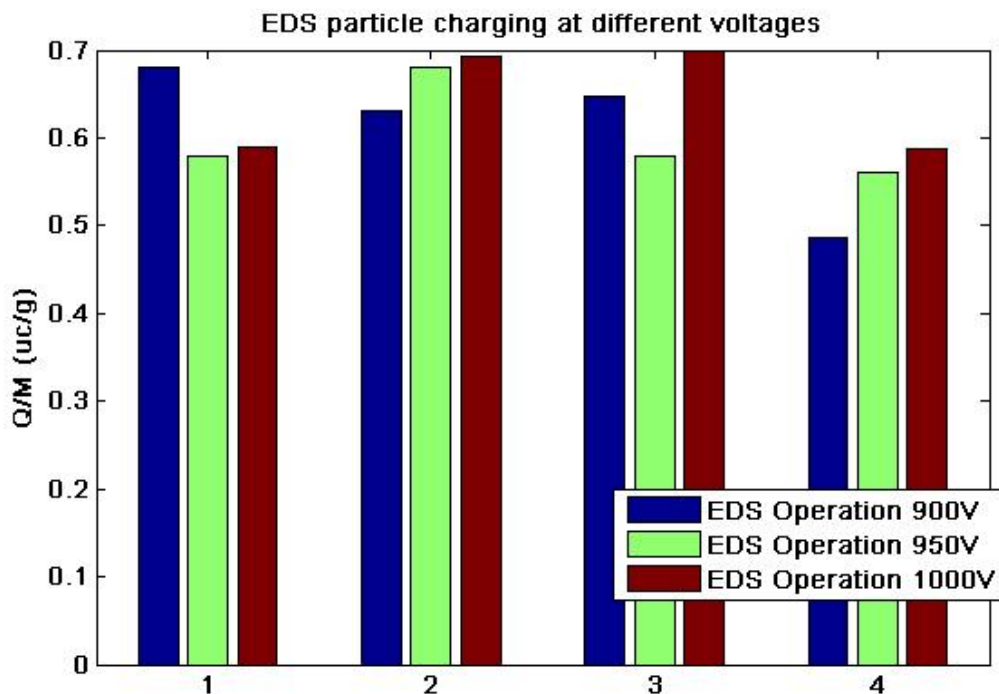


Figure 3-5: Charge to mass ratio for applied voltages with Dubai desert sand.

The results from varying the voltage show that the net charge to mass ratio on the sand particles collected in the Faraday cup when varying voltages does not change greatly when a large number of particles are removed from the surface of the test panel. When the applied three phase voltage is below 900 volts, the sand on the surface of the panel does not move, and is not collected in the Faraday cup. While these particles may not be highly charged, the electric field strength is also not sufficient to move the particles from the surface. This suggests that when the particles are affected by the non-uniform electric field created by the applied voltage, the particles being removed from the test panel are near the saturation charge of the sand particles. The maximum charge a particle can gain through tribocharging is shown in equation 3.1, where q_{max} is the maximum charge on the particle, ϵ_1 is the dielectric constant of the medium the particle is in, d is the particle diameter, and E_1 is the breakdown voltage of air (Sims et al., 2003).

$$q_{max} = \epsilon_1 \pi d^2 E_1 \quad (3.1)$$

The percent of saturation charge for each trial was plotted in a bar graph, using the calculation for maximum charge for the mean particle diameter from equation 3.1. In figure 3-6, the percent of saturation charge for the net charge was calculated and plotted for the trial where the applied three phase voltage was set to 900 volts. In these trials the net charge measured for the particles is approximately 65 percent of saturation charge.

As the three phase voltage applied to the electrodes was increased to 950 volts, the net charge to mass ratio was a similar magnitude as the other trials. As shown

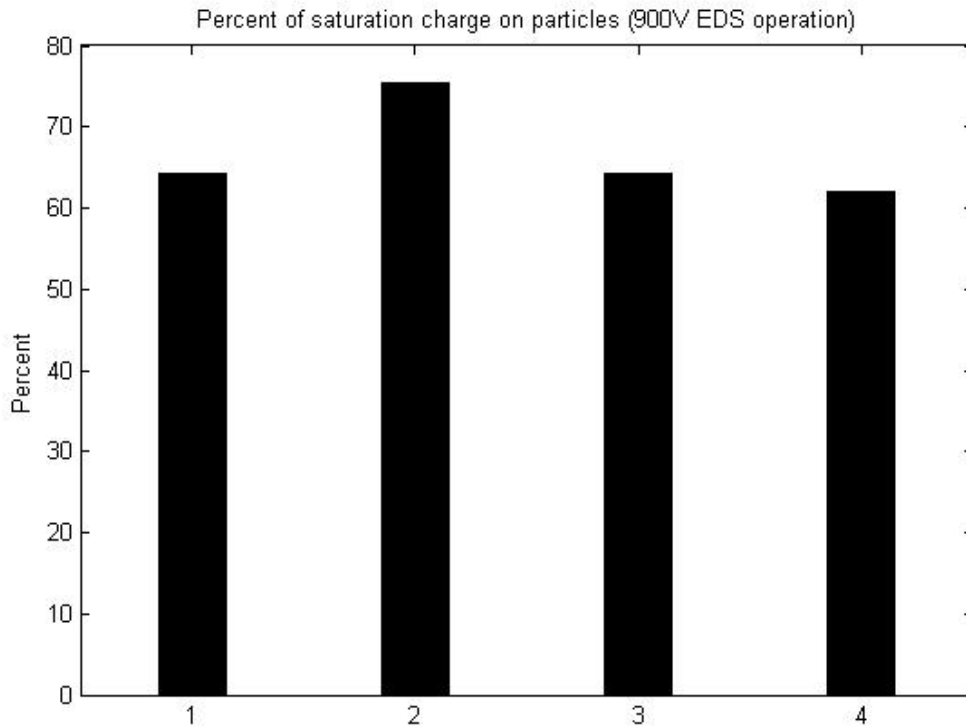


Figure 3-6: Graph showing the calculated percent saturation charge based on the mean particle diameter and the net charge measurement for 900 volt applied voltage tests.

in figure 3-7, the bar graph shows the percent of saturation charge for the trials ran at 950 volts. These trials show again approximately a 65 percent saturation charge.

In the final trial where a three phase, 1000 volt signal was applied to the electrodes, the net charge to mass was similar to the other trials. Figure 3-8 shows the plot of percent of saturation charge for each of the trials at 1000 volts. Again, these trials show approximately 65 percent of saturation charge for the net charge on the particles for the mean particle size in the test sample.

The previous graphs in figures 3-6, 3-7, 3-8 show from the net charge of the particles falling into the Faraday cup, the particles experience a high net positive

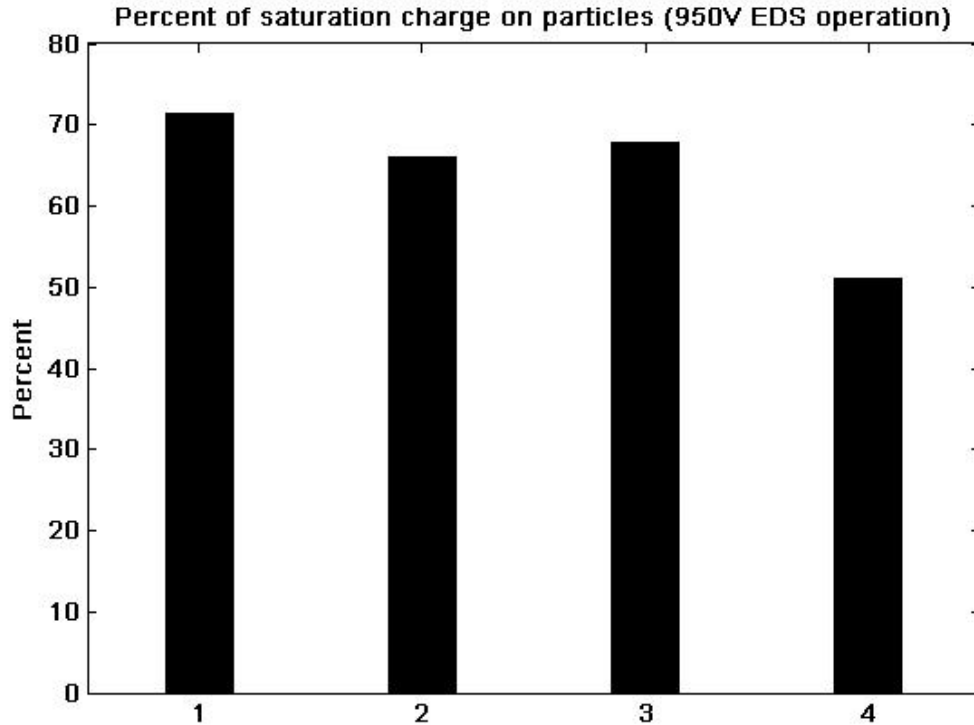


Figure 3·7: Graph showing the calculated percent saturation charge based on the mean particle diameter and the net charge measurement for 950 volt applied voltage tests.

charge when the voltage is applied and the particles are in a non-uniform electric field. When this field is not applied and the particles only experience mechanical movement causing tribocharging, the net charge measured is a very small negative charge to mass ratio. By applying the non-uniform field, the particles experience a dielectrophoretic force as shown in equations 3.2 and 3.3. (Jones, 2003) In these equations, ϵ_1 is the dielectric constant medium the particle is in, which in this case would be air, ϵ_2 is the dielectric constant of the particle, K is the Clausius-Mossotti factor, and k is the wavenumber as defined by $k = 2\pi/\lambda$.

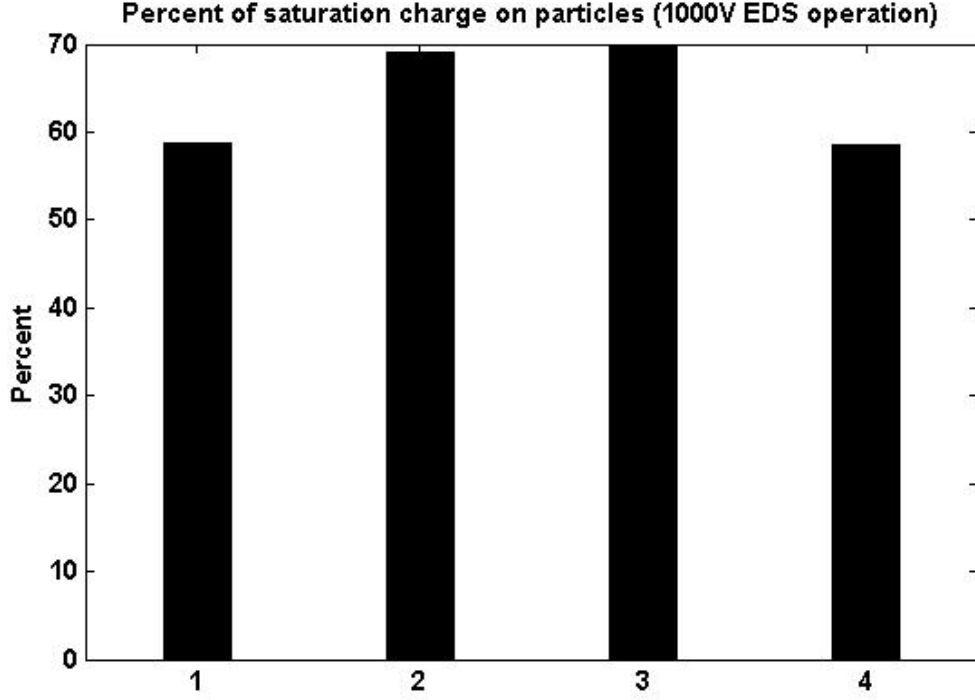


Figure 3-8: Graph showing the calculated percent saturation charge based on the mean particle diameter and the net charge measurement for 1000 volt applied voltage tests.

$$F_{DEP_x} = -4\pi\epsilon_1 r^3 k E^2 e^{-2ky} \times [\text{Im}[K^{(1)}] + \frac{2k^2 r^2}{3} \text{Im}[K^{(2)}] + \dots] \quad (3.2)$$

$$F_{DEP_y} = -4\pi\epsilon_1 r^3 k E^2 e^{-2ky} \times [\text{Re}[K^{(1)}] + \frac{2k^2 r^2}{3} \text{Re}[K^{(2)}] + \dots] \quad (3.3)$$

$$K = \frac{\epsilon_2 - \epsilon_1}{\epsilon_2 + 2\epsilon_1} \quad (3.4)$$

The dielectrophoretic forces acting on the particle are much smaller in magnitude than other forces acting on the sand particles, such as the Coulomb force, electrostatic image force, and gravitational force. The dielectrophoretic force acts to cause a

rotational motion on the particles, since it is operating as a translational force of the imaginary and real components of the non-uniform field. By adding the rotational motion of the dielectrophoretic force acting on the sand particles in the applied electric field, the sand particles become highly charged and are removed from the surface of the panel.

3.3 Effects of humidity on sand charging on electrodynamic screens

The effect of humidity on charging properties of various materials has been documented in numerous studies (Sharma et al., 2003) (Sims et al., 2003). As the humidity increases the sand particle charge decays faster, as shown in table 2.2. Particles that are removed from the surface of the electrodynamic screen are charged, and experience a coulomb force that is proportional to the charge of the particle. While particles with lower charge will experience less Coulomb force and will be less likely to be removed from the surface of the electrodynamic screen, particles with higher charge will have a greater Coulomb repulsive force and will be more likely to be removed.

To study the effect of relative humidity on the effectiveness of clearing dust from solar mirrors using electrodynamic screens, the panels were tested in a humidity controlled environment at varying levels of humidity and the charge to mass was measured as the sand particles were removed from the surface of the panel. The test panel was set up in a humidity controlled chamber as shown in figure 3.1. The test panel was inclined to a 30 degree angle, sand samples from Dubai that had been

sieved and dried were placed into a sieve with a vibrating motor attached. Once again a Faraday cup connected to an electrometer was placed under the edge of the test panel, and a metal insert was placed into the Faraday cup to allow for mass measurements after dust collection. The humidity was set to a fixed percentage using the environmental chamber's controls and was left for 30 minutes at the set humidity value. After the humidity was set, the vibrating sieve was activated and sand was deposited onto the surface of the test panel.

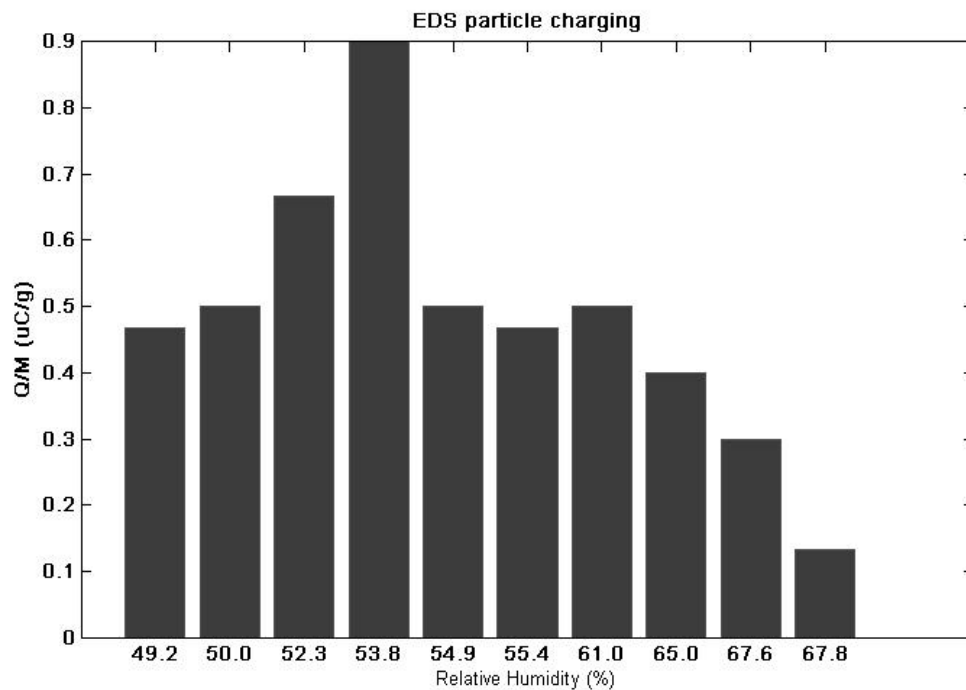


Figure 3-9: Plot of charge to mass measurements for Dubai sand at varying humidity levels

After sand was deposited onto the test panel, a three phase, five hertz, 1000 volt signal was applied to the panel for one minute. The dust that was removed from the panel was collected in the Faraday cup, and the final net charge from the electrometer was recorded. The metal insert from the Faraday cup was removed and

the change in mass was measured using a balance and recorded. After testing at several humidity ranges, the values were plotted, as shown in figure 3-9. The charge to mass measurements after 50 percent relative humidity show a sharp decrease in charge to mass, along with a sharp decrease in the amount of dust removed from the surface of the test panel. At higher relative humidity conditions, the effectiveness of particle charging is diminished, which leads to a decrease in dust removal performance.

Chapter 4

Modeling Optical Power Losses

4.1 Modeling power losses due to dust loading

After determining properties of sand samples being tested, a method of modeling the power losses due to dust accumulation must be considered. Studies have shown that dust accumulation in desert areas has a correlation with power output of solar installations (Sarver et al., 2013),(Al-Hasan, 1998),(Offer and Goossens, 2001),(Niknia et al., 2012),(Goossens and Offer, 1990). The grain size of sand can be shown to correlate with obscuration of light incident onto a solar module, which in turn will relate to the output power in solar cells, specular reflection in CPV mirrors, or concentrated light incident on a CSP module. The size of the particle relates to the optical cross-section that will obscure light. This obscuration of light can be represented and modeled through the Beer-Lambert Law, by modeling the dust accumulation on the surface of a solar module as a concentration of particles with a given size distribution. (Mazumder et al., 2003).

The equation for the Beer-Lambert Law is shown in Eq.(4.1).

$$I = I_0 e^{-NA_p Q_{ext}} \quad (4.1)$$

In this equation, N represents the concentration of sand particles on the solar

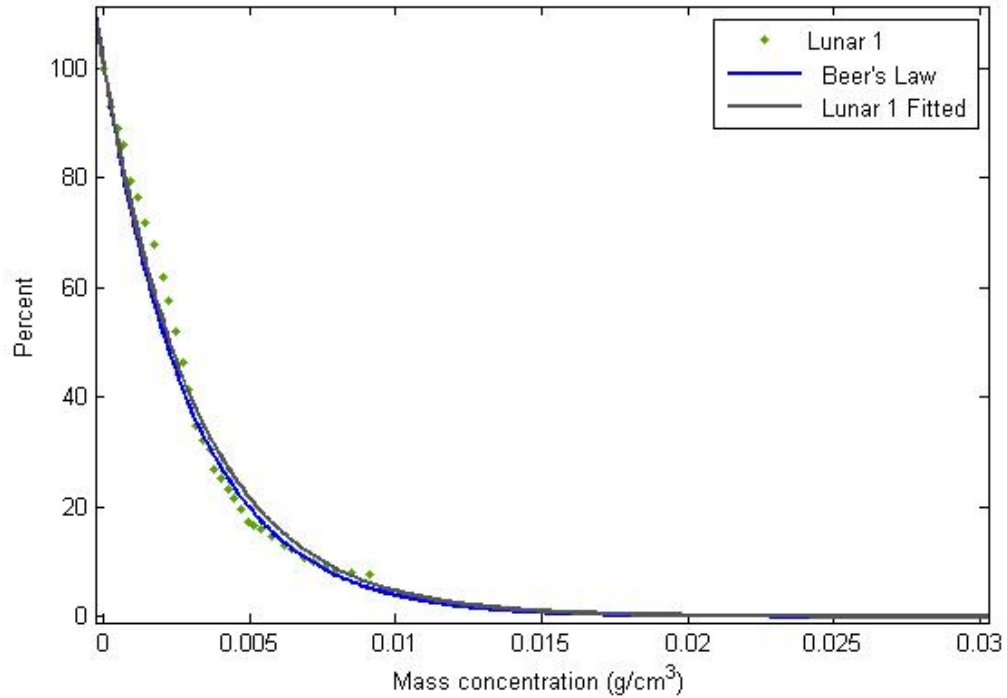


Figure 4-1: Dust deposition of JSC-1A Lunar regolith modeled on photovoltaic module along with predicted data based on particle size distribution

module surface in particles per unit area, A_p is the optical cross-section of the particle in m^2 , and Q_{ext} is the extinction coefficient for the given material. Figure 4-1 shows a graph of JSC-1A Lunar regolith deposited onto a surface of a solar module while measuring normalized power output with respect to the maximum power measured and deposited dust mass. This data was plotted with Beer's law and curve fitted.

For calculating specular reflection, which is the measure of reflected light not diffused by a reflection surface, scattering effects of dust will become more pronounced by creating diffuse light that will stray from the solar collector after reflection. In addition to this, dust accumulation on the surface of solar mirrors will cause incident solar radiation to pass through the accumulated dust layer twice, increasing the loss

due to dust accumulation. To account for this in calculation, the formula will show twice the initial propagation, since the light propagating through the dust is calculated by dust mass concentration values, it will properly account for any chances light has of interacting with any particles in this distribution.

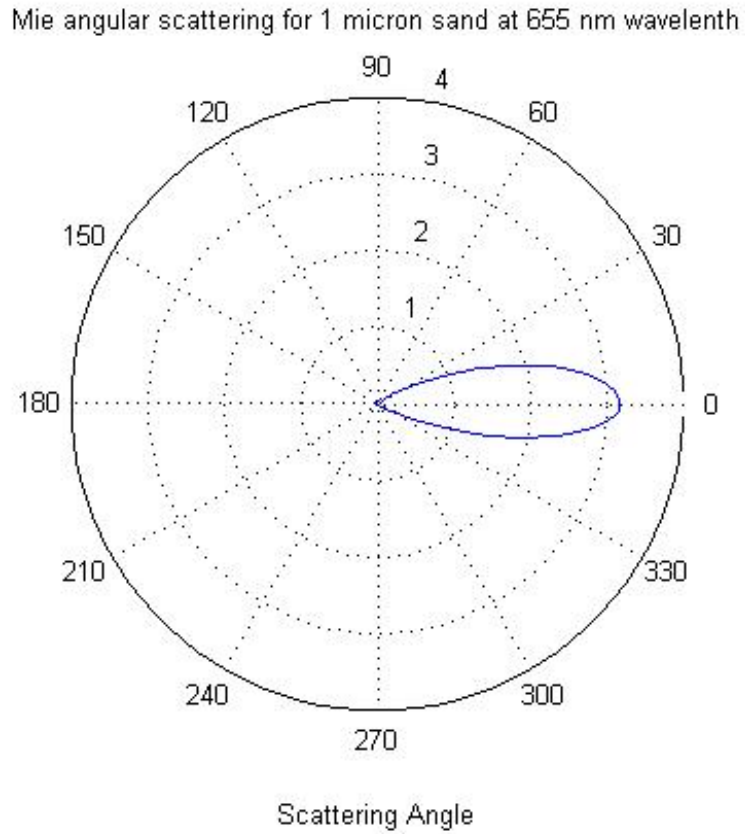


Figure 4-2: Scattering plot calculated for 1 micron sand at 655 nanometer wavelength source.

To establish a model for specular reflection measurement for accumulated dust on solar reflectors, Mie solution to Maxwell's equations can be employed to calculate scattering coefficients for sand grain sized in different concentrations for given wavelengths (Qasem et al., 2014). Using Matlab, values of scattering coefficients were determined for studied cases of specific sand sized and depositions. A generated

plot of scattering angle for a 1 micron sand particle is shown in figure 4.2. The values from the solution in Matlab were used to determine a scattering and absorption coefficients, Q_{sca} and Q_{absp} to replace the overall extinction coefficient in equation (4.1). The specular reflection is shown in equation (4.2), using a coefficient of 2 for the reflected light attenuation after hitting the mirror surface, and the expanded attenuation coefficient determined through the Mie solution results. While this model currently only looks at a 655nm wavelength due to the model testing procedures used, this method can be expanded to include the complete solar spectrum.

$$R_{spec} = I_0 e^{-2NA_p(Q_{scat}+Q_{abs})} \quad (4.2)$$

A manufactured dust sample, JSC-1A Mars regolith test dust, was deposited onto a highly reflective borosilicate glass mirror while measuring specular reflection and accumulated dust mass. The graph is shown in figure (4.3).

The losses in specular reflection were also studied as a function of angle of incident light and particle size. A FRED ray tracing model was developed to observe the scattering of particles. In this model, dust particles in concentration of $1.9g/m^2$ with particle diameters of 3, 5, 10, 20, and $30\mu m$ were added to a simulated dust removal screen and the ray tracing simulation was run at 15, 30 and 60 degree incident angles to observe the effect on the energy collection efficiency. The effect of particle size with a given dust concentration at varying angles of incidence is shown in figure 8. This shows a relationship between smaller particles in lower mass concentrations and the decreased specular reflection as smaller particles accumulate on a concentrating solar mirror.

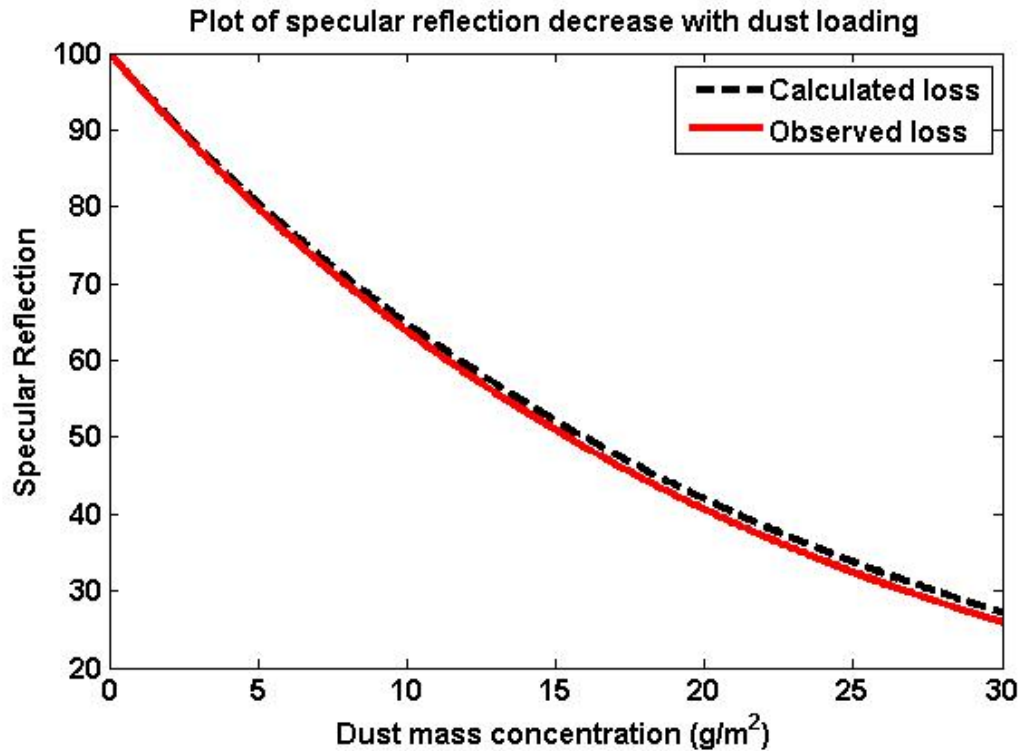


Figure 4.3: Comparison of specular reflection values with calculated results.

4.2 Reflection Losses Due to Electrodynamic Screen Integration into Solar Mirrors

In addition to losses due to dust accumulation, adding an electrode grid onto the solar facing surface of a module will cause some degree of specular reflection loss, even with semi-transparent electrodes. Along with the electrodes, the module will need a protective dielectric covering to insulate the electrodes and protect them from weathering effects (Mazumder et al., 2003). Each layer will contribute to a decrease in specular reflection by adding to diffused reflection and absorption as the incident light propagates through the layers to the mirror, and back again. A cross sectional area of the panel is shown in figure 1.2, which shows the transparent dielectric layer (borosilicate

glass, acrylic, or urethane films), the embedded electrode grid, a borosilicate glass substrate, and finally a mirrored reflector.

Ray tracing analysis has been successfully used in modeling and evaluating solar photovoltaic and concentrating solar systems, and has been developed into several commercial and publicly available software packages (Gregory and Koshel, 2006), (Ho,), (Wendelin,). For this modeling application, FRED Optical Engineering Software by Photon Engineering has been chosen to model the device. To model the design in FRED, arrays of electrodes with material specifications were created in FREDs CAD environment, with electrodes patterned with a Gaussian shaped profile to approximate the profile of electrodes when patterned with screen printing technology. The printed electrodes height and width were measured using a Tencor Alpha Step 500 surface profilometer, and this data was fitted into the Gaussian approximation for electrode profiles used in the model. The light sources used for modeling was given as a single wavelength 655nm source, which is the same wavelength used in the specular reflectometer for testing the panels. The source was placed at a 15 degree angle of incidence from the modeled EDS panel. The simulation was run with 2,000,000 rays traced. The results from the FRED simulations compared with the measured specular reflectivity of the panels is shown in table 4.1.

After fabrication of the dust removal mirrors was completed, each module was tested for specular reflection using a non-contact specular reflectometer with 655nm wavelength source, 15 degree incidence angle, and 1.4 degree acceptance aperture. The mean specular reflection was taken from five dust removal modules with chrome electrodes, and the specular reflection for the PEDOT:PSS electrodes was taken as a

Material	Electrode Width	Electrode Spacing	Specular Reflection
PEDOT:PSS (simulation)	$100\mu m$	$700\mu m$	94.4
Chrome (simulation)	$100\mu m$	$700\mu m$	84.8
PEDOT:PSS (measured)	$100\mu m$	$700\mu m$	92.4
Chrome (measured)	$100\mu m$	$700\mu m$	81.9

Table 4.1: Simulated specular reflection results with laboratory measured initial (clean) specular reflection. Electrode widths and spacings were modeled after the initially produced panels.

mean value from four measurements on a single module.

Chapter 5

Development of Non-Contact Specular Reflectometer

5.1 Introduction

In development of self-cleaning solar mirrors, a method was needed to continuously measure the change of specular reflection without changing the properties of the surface being measured. Commercially available devices require a measurement device to contact the surface of the reflector to measure the specular reflection of a mirror. Contacting the mirror's surface for measurement would not allow for measurement of change of specular reflection after mirrors have been soiled, but before being cleaned. These needs for continuous measurement of specular reflection via non-contact method drove the design of the device described in this chapter.

5.2 Design of device

The design of the device was centered around the concept of allowing continuous testing and operation of solar mirrors while monitoring specular reflectivity. These tests are specifically created to test dust deposition, and the effect of dust on the degradation of solar mirrors. Other specular reflectometers are designed for portable use, which require the reflectometer to rest on the surface of the test sample(DS

reference, SNL test reference). These portable reflectometers require contact points to establish a set distance way from the solar reflector to create a correct measurement angle. A portable specular reflectometer, commercially available from Devices and Services Corporation is shown in figure 5.1. While placing the measurement device directly on the reflector surface is an effective method of establishing the deviation of the reflected beam, it interferes with measurements of dust loading by contacting the surface of the reflector.

To allow the device to keep the angular tolerances for specular reflectivity measurements, the optics and test bed were designed to be stationary, instead of on a moving stage in the hand held design. By this stationary design, the reflecting surface of the mirror would stay at a constant angle with reference to the transmitting (LED source being sent to mirror) and receiving optics (optical detector). The angular tolerance of the device can be set by the precision of the machining for the frame and the precision of the receiver optical adjustments. A CAD rendering of the device is shown in figure 5.2.

The source used is a 655nm collimated LED source with a current controlled power supply. Since in an LED device, current control will be proportional to the intensity of the output, the current controlled power supply allows for a very stable beam output. The source can output a beam of stable intensity and wavelength over much of the output range of the LED. The 655nm wavelength source is a good approximation for the mid-range energy for a solar source. The collimated LED shows minimal divergence over the 30 centimeter total beam propagation distance, from the source to the reflection surface, and to the receiving optics. The solar reflector is



Figure 5-1: Image of a hand-held specular reflectometer, D& S model 15R, made by Devices and Services Company. The reflectometer is placed onto the surface that is to be tested, which can interfere with dust on the solar mirror that is being tested.

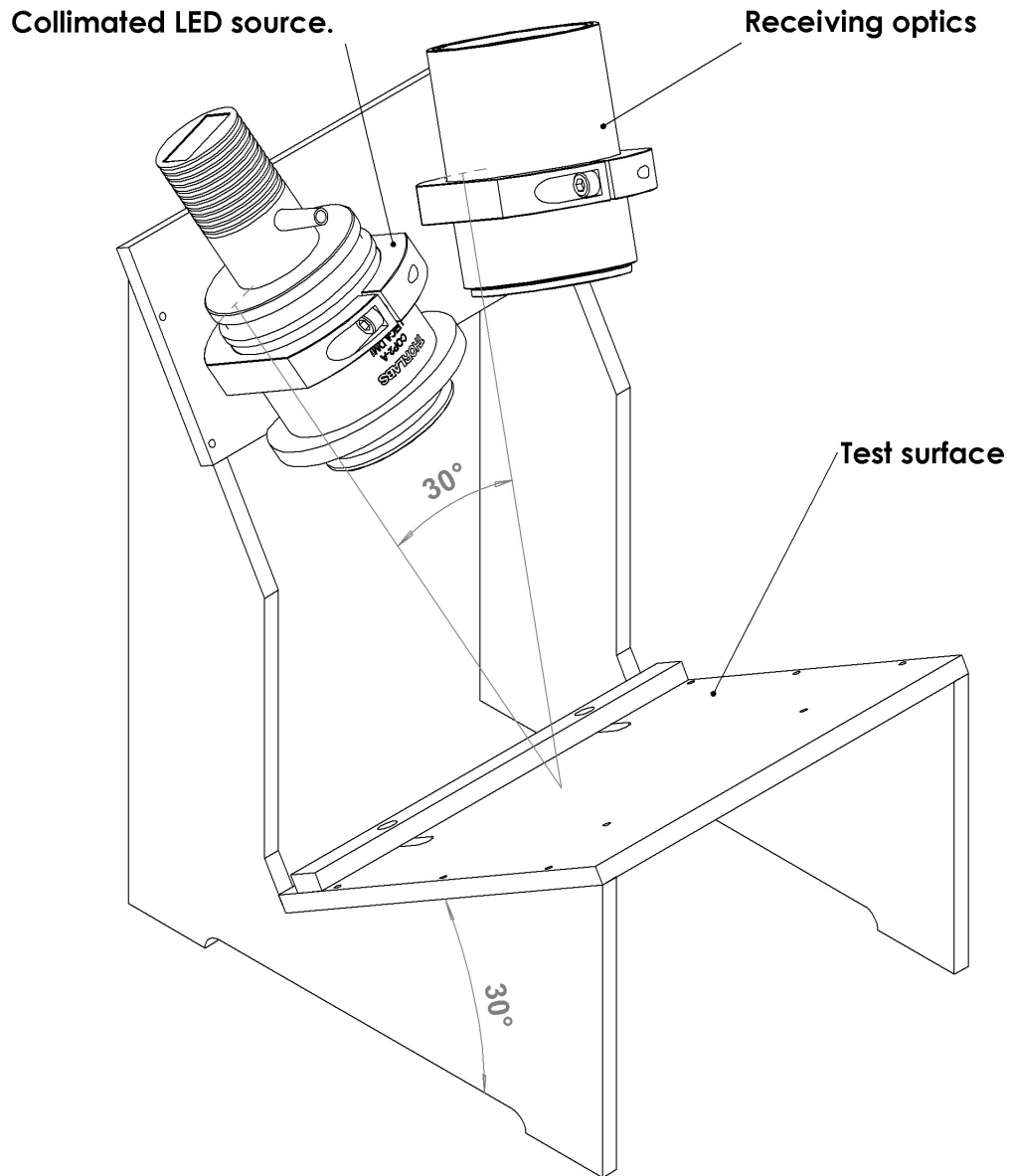


Figure 5-2: Rendering of the specular reflectometer, which shows the collimated LED source, testing surface, and receiving optics, with the optical angle between the source and receiver.

placed on a table that is positioned at an angle of 30 degrees to the horizontal, which would simulate an angled surface in a solar installation. This surface is positioned 15

centimeters from the receiving and transmission optics, and set to a 15 degree angle of incidence from the source and 15 degree angle of incidence to the receiving optics.

The receiving optics consist of a lens tube, neutral density filter, diffuse blocking aperture, focusing lens, and an optical detector. The neutral density filter acts to block a portion of the incoming light, allowing the optical sensor to work within the linear range for the desired specular reflection range. This will allow for stability in the optical source and good sensor resolution without changing optical detectors or sources. After the light reflected from the test surface has passed into the neutral density filter, the diffuse blocking aperture is used to block any diffuse light. The aperture is selected to give a 25 milliradian angle of acceptance for light reflected from the test surface. This aperture can be changed to give a tighter constraint on specular reflection, as needed. After the specularly reflected light passes through the diffuse blocking aperture, the light is then focused by a lens into the optical detector. The optical detector produces a voltage readout with an internal transimpedance amplifier with a photodiode sensor. The detector has a high sensitivity in the 655nm wavelength range.

Since the output of the optical detector is read out in voltage, the signal has to be calibrated to specular reflection. Multiple mirrors of varying quality, from 50 percent specular reflection, to 96 percent specular reflection were tested with the device and the voltage reading was noted. For each voltage reading, the sensor averaged thirty samples over five seconds to allow for an average of values that could change due to small unaccounted for variations in the signal. The samples were also tested with a D&S 15R specular reflectometer with the 25 milliradian aperture setting.

The specular reflection measurements for each sample were noted. The voltage and reflection values were plotted in Matlab and curve fitted to give an equation to relate the specular reflection to the voltage output of the sensor. The plot of the voltage values and curve fitted equation for specular reflection is shown in figure 5-3.

$$SR = 0.49 * Voltage - 0.87 \quad (5.1)$$

The curve fitted equation for specular reflection from voltage output of the sensor is shown in equation 5.1. For each test mirror used for calibration, The mirror surfaces were cleaned with an isopropyl alcohol solution and the specular reflection was measured five times with the D&S 15R and the measurements were averaged to account for any small variations in specular reflection across the surface of the mirror. After the initial sensor calibration values were taken and the voltage to specular reflection equation was produced, the output value of the sensor was calibrated to the maximum value range for specular reflection using a highly reflective calibration sample. The calibration sample was placed on the specular reflectometer test bed, and the collimated LED source was adjusted while reading out the specular reflection of the reflectometer. The specular reflection was matched to the calibration sample's value before each test to ensure proper calibration of the device.

5.3 Experimental setup

After the specular reflectometer has been calibrated and tested with sample mirrors, the device is tested with dust loaded mirrors and electrostatic self-cleaning mirrors. Self-cleaning mirrors are constructed from borosilicate glass substrates, parallel elec-

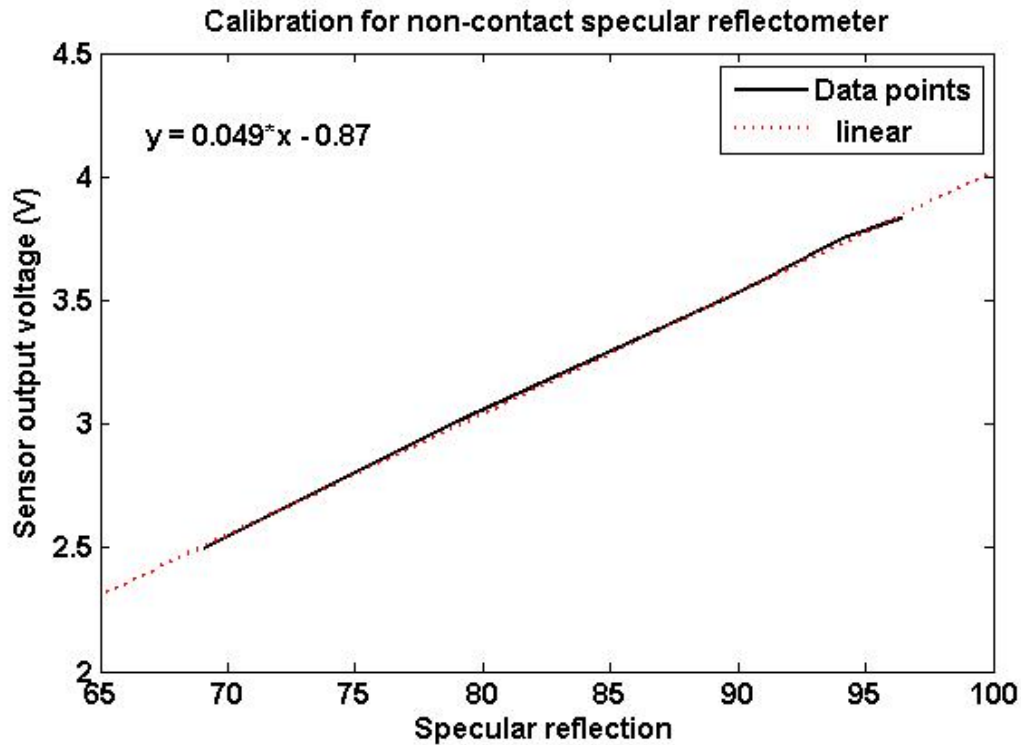


Figure 5-3: Initial calibration data for noncontact specular reflectometer, based around measurements from multiple mirrors with varying quality of specular reflection

trodes, and a transparent dielectric material encapsulating the electrode materials. The borosilicate glass substrate is fixed to a highly reflective mirror, in the case of these tests, 3M 1100 Mirror film. For only dust loading tests on mirrors, the mirrors used are borosilicate glass substrates with 3M 1100 Mirror film fixed to the back surface of the substrate. A cross-sectional diagram of the electrodynamic dust removal mirror is shown in figure 1-2. Dust removal mirrors are attached to high voltage three-phase power supplies and the three phase voltage is applied to the electrodes to create an electrostatic traveling wave to remove the dust from the mirror's surface.

The reflectometer is placed into an environmentally controlled chamber which keeps humidity at a constant level, controls external winds, and minimizes dust con-

tamination, where the mirrors can be tested under controlled conditions. Dust deposition is controlled with the use of a fluidized bed dust deposition system, which creates a flow of dust that can be directed toward the testing surface, and allows for the rate of flow to be controlled by the rate of airflow into the device. Because of the constant measurement ability of the non-contact specular reflectometer, the deposition of dust onto the mirror surface can be continuously measured as dust is deposited and removed. As the panels are being tested, the specular reflection and humidity readings are monitored on a desktop computer.

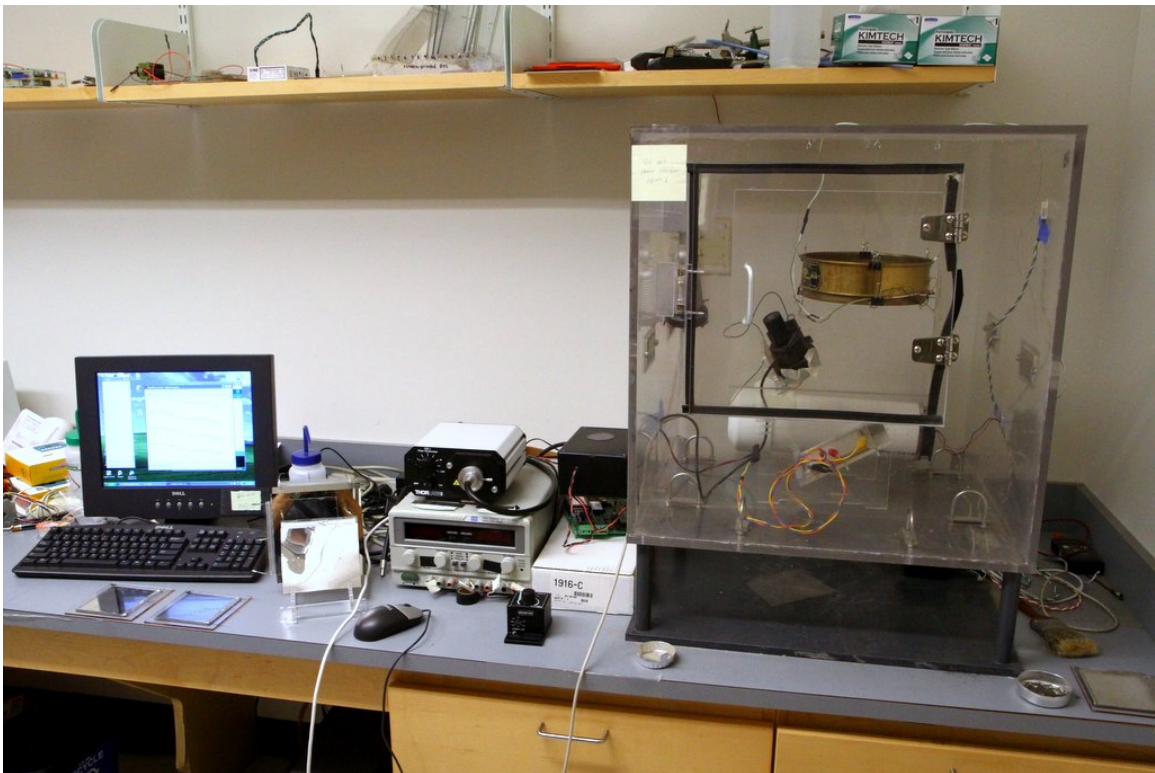


Figure 5-4: Testing chamber for controlling environmental conditions and containing dust deposition for testing solar mirror specular reflection under dust loading conditions and self-cleaning performance of electrostatically enhanced mirrors.

In the testing procedure, mirrors are initially tested while clean, after being

cleaned with isopropanol, panels placed into the chamber and the specular reflection is recorded. For simple mirrors, the decrease in specular reflection is recorded as the dust deposition accumulates onto the surface. For self-cleaning mirrors, the cleaned mirrors are placed into the testing chamber onto the non-contact specular reflectometer's testing bed, and an initial specular reflection measurement is taken. After the initial measurement is recorded, the fluidized bed is activated and a small amount of dust is deposited onto the surface of the self-cleaning mirror. The soiled mirror's specular reflection is recorded and the power supply for the mirror is activated for one minute at 1kV and 5Hz. After one minute the power supply is deactivated and the specular reflection of the mirror is recorded. The test is then repeated for ten trials to establish a repeatable performance of cleaning for the self-cleaning panel.

5.4 Results and discussion

Mirrors with chrome electrodes, PEDOT:PSS electrodes, silver nanowire electrodes, and borosilicate glass mirrors with no electrodes were tested using the non-contact specular reflectometer. The different electrode materials have varying degrees in transmission for the different materials, which causes different specular reflection for the initially clean mirror measurements. For testing with control mirrors, dust is loaded and specular reflection is measured, along with dust mass concentration measurements taken by microbalance mass measurements of the mirror. The results of the dust loading on the mirror are shown in figure 5-5. The figure shows the non-contact specular reflectometer data giving consistent decrease in reflection with additional dust mass concentration.

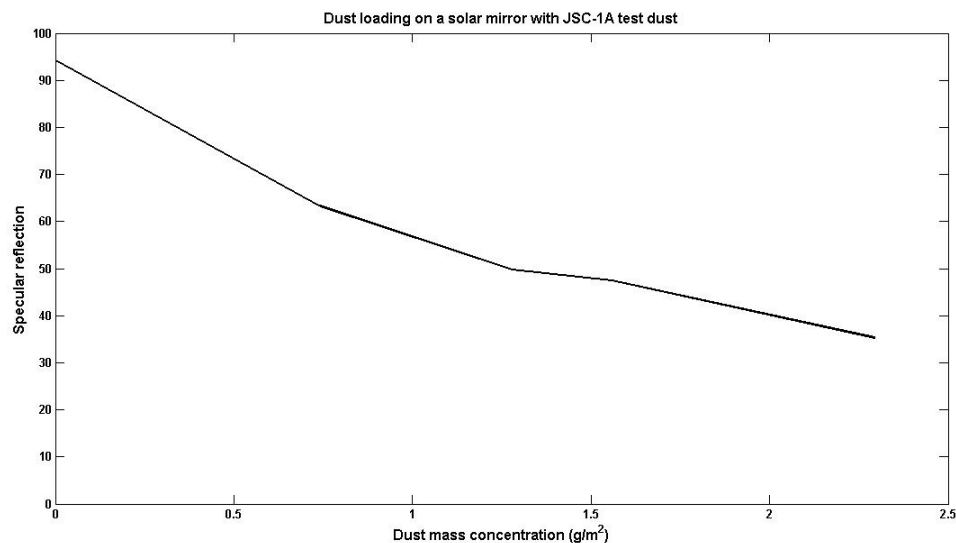


Figure 5-5: Graph showing dust loading on a mirror with non-contact specular reflectometer taking measurements of reflection as JSC-1A Mars simulant test dust is used.

The use of the non-contact specular reflectometer in this method allows for measurements to be taken without changing the position or concentration of dust as it is deposited onto the surface of the mirror. This method of specular reflection measurement can provide accurate results of dust deposition rates and mirror soiling in real time without disturbing the surface being tested. The following sections discuss the results of specular reflection testing for solar mirrors with self-cleaning properties due to embedded electrodes of three different materials; PEDOT:PSS, Chrome, Silver nanowire.

5.4.1 PEDOT:PSS Electrodes

The panels tested were fabricated by screen printing PEDOT:PSS electrodes onto borosilicate substrates and encapsulated with acrylic film approximately 50 micrometers thick. This method produces a thin, narrow electrode with a parabolic profile.

The electrode width varies due to the bleed out of the ink, and has a mean electrode width of 184 microns and standard deviation of 26.3 microns, and a mean electrode height of 960 nanometers and standard deviation of 450 nanometers. The PEDOT:PSS ink at this thickness has transmission in the 650 nanometer range of around 80%, allowing for moderate transparency and good conduction for electrostatic purposes.

The initial specular reflection for the panel tested was 85.6%, and the panel's specular reflectivity decreased as dust was deposited onto the panel in the sequential trials. The trials are shown in 5-6, where the three lines represent the value of specular reflection before depositing dust, after dust deposition, and after the electrodynamic screen activation, in black, red, and blue lines respectively. The trials were conducted sequentially, with no cleaning or disruption of the mirror's surface, except for the electrodynamic screen activation. In each case a large portion of the dust loaded onto the surface was removed during each trial, but some remained. After the tenth trial, the final specular reflection value recorded was 71.8%.

5.4.2 Chrome Electrodes

The chrome electrode mirrors were fabricated using a photolithographic process, where the pattern was written to the surface of the substrate using a laser writer, and then unwanted surfaces were removed through chemical etching. This process creates very precise electrode with accurately defined width and height. Since the pattern is chemically etched, the electrode profile is of a rectangular shape, unlike the Gaussian profile from the screen printing method. The mean electrode width was

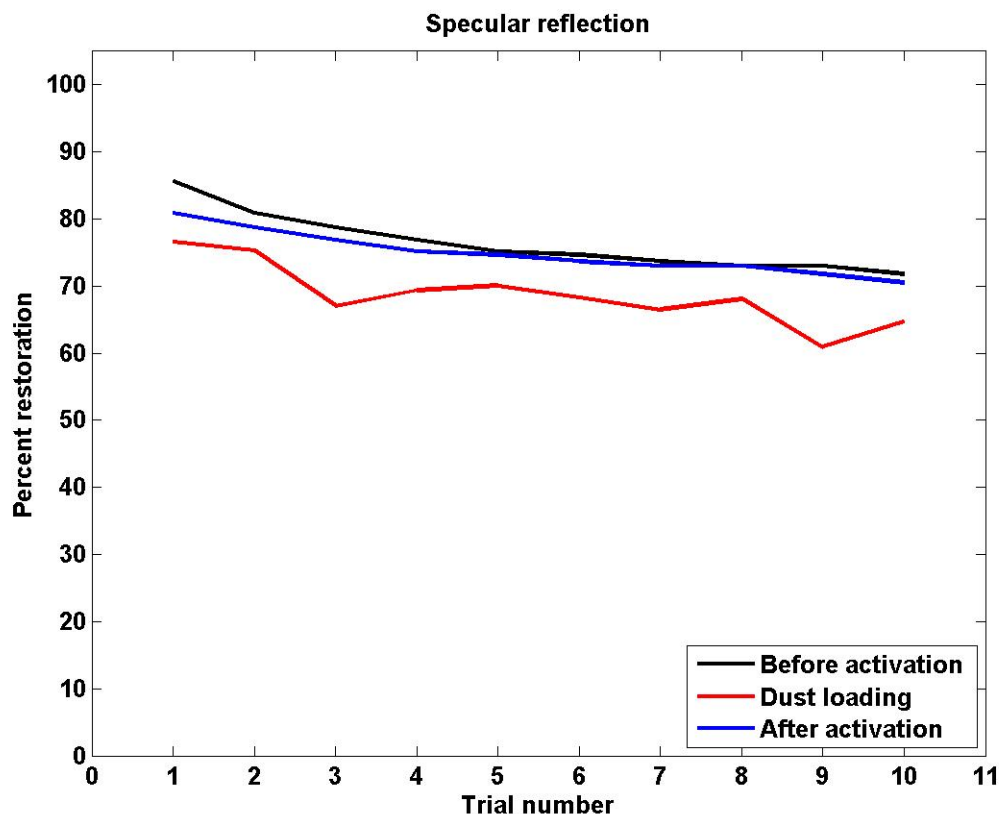


Figure 5-6: Graph showing dust removal performance of PEDOT:PSS electrodes taken with non-contact specular reflectometer over ten dust loading and cleaning cycles in an environmental chamber.

102 micrometers with a standard deviation of 1.4 micrometers, and the mean height of the electrode was 109 nanometers with a 13 nanometer standard deviation. After the fabrication of the electrodes, a 100 micrometer borosilicate glass layer was used to encapsulate the electrodes, and the substrate was fixed to a mirrored surface to create the self-cleaning mirror assembly.

For the initial specular reflection value taken with a clean mirror surface, a value of 88.9% was recorded for the mirror assembly. As the test began the specular reflection decreased as dust was deposited, increased as dust was removed when the electrody-

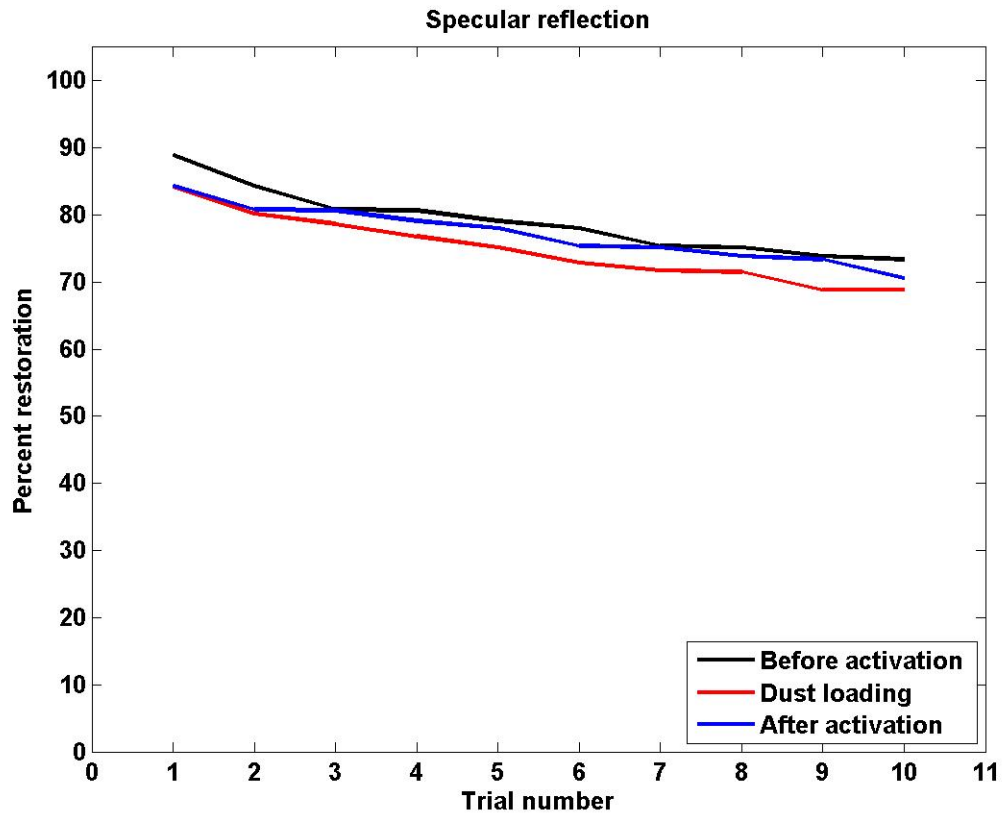


Figure 5·7: Graph showing dust removal performance of chrome electrodes taken with non-contact specular reflectometer over ten dust loading and cleaning cycles in an environmental chamber.

dynamic screen surface was activated, and slowly declined through the following trials. A plot of the trial is shown in 5·7, where the specular reflection reading before dust deposition is shown in black, the reading after dust deposition is shown in red, and the reading after electrodynamic screen activation is shown in blue. For the duration of the trials, the panel was undisturbed after each loading, with the exception of the activation of the dust removal electrodes, and each trial was performed sequentially. After the tenth trial the final specular reflection reading after electrode activation was 70.6%.

Electrode width	Electrode spacing	Vertical specular reflection	Horizontal specular reflection
25	800	90.1	91.5
50	500	80.2	84.7
50	800	87.7	87.9
200	700	77.9	78.3
300	400	48.9	57.5
300	600	68.6	69.2
300	900	65.9	73.5
500	500	58.3	62.6
500	800	55.7	68.9
600	400	51.8	53.6
800	300	38.2	48.4

Table 5.1: Table showing electrode width and spacings for photolithographic chrome panels, along with the specular reflection values for two different orientation of electrodes

Since the photolithographic process allows for rapid development of alternate electrode geometries, multiple electrode geometries were tested. Panels with varying electrode widths and spacing were developed, and the effect of changing electrode geometry on specular reflection can be shown. As the mirror surface is covered by more electrode area, the specular reflection decreases, giving an optimal specular reflection when the electrodes are very narrow and far apart. The panels and the specular reflection values recorded are shown in table 5.1.

Along with the varying specular reflection due to the electrode width and spacing, the panels show a specular reflection dependence on electrode orientation. In cases where the electrodes are oriented horizontally to the earth, specular reflection is higher

than when the electrodes are oriented vertically. This measurement is readily apparent due to the non-transparent chrome electrodes shading more of the mirrored surface than other materials. The reflectometer's collimated beam is oriented in a way such that the angle of the reflecting beam is in the same plane with horizontally oriented electrodes. This allows the light that would normally be blocked by a reflection from the mirrors surface to only interact with the chrome electrodes at the incidence. When the electrodes are oriented vertically, the angle of incidence of the collimated beam is transverse the plane of the parallel electrodes, causing the reflected beam to be blocked by underside of the chrome electrodes. With electrode materials that have high transmittance, such as PEDOT:PSS and silver nanowire ink, the shading effect is less pronounced because the light is transmitted instead of reflected by the electrode materials.

5.4.3 Silver Nanowire Electrodes

The mirrors with silver nanowire electrodes were fabricated using the same screen printing method as the PEDOT:PSS electrodes, and have similar geometric characteristics, like a gaussian profile, wider electrode width than chrome electrodes, but have a smaller electrode height due to a thinner consistency of ink. The silver nanowire material in the dilution used has a transmission over 90% in the 650 nanometer wavelength band, and a very high conductivity in thin films. The electrodes were printed directly onto the borosilicate substrate, and the electrodes were encapsulated with optically clear adhesive and 100 micrometer borosilicate glass in the same method as the chrome electrodes. After the electrodes were encapsulated, a highly reflective

mirror film was fixed to the back of the substrate to complete the mirror assembly.

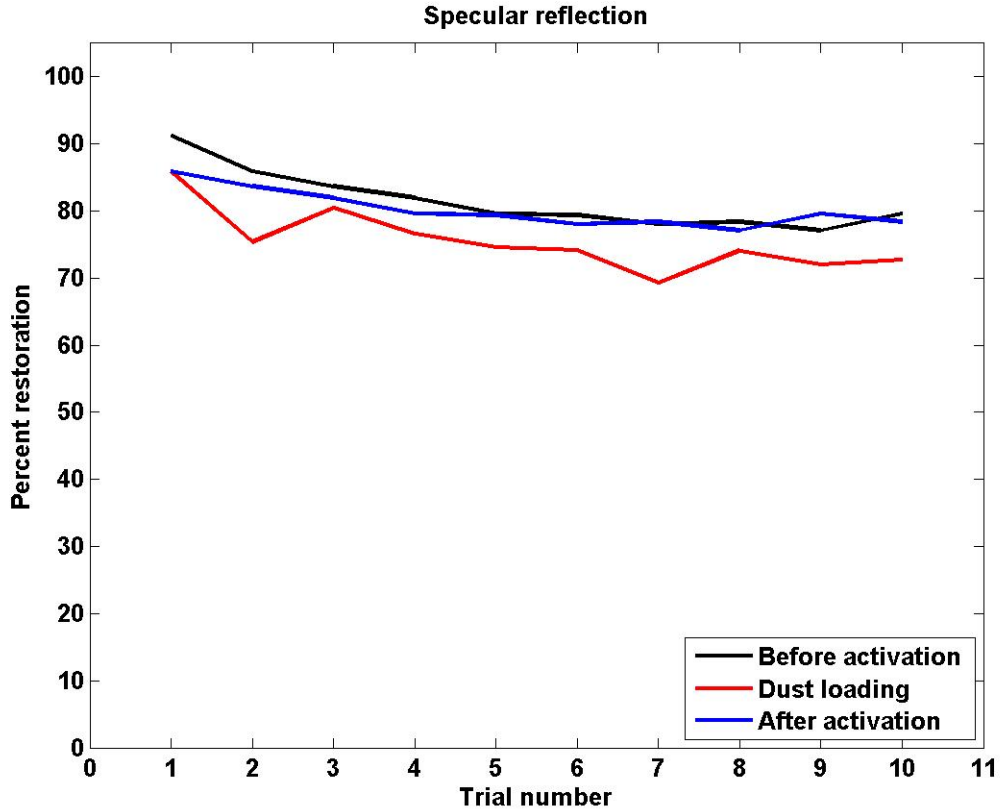


Figure 5-8: Graph showing dust removal performance of AG-NW electrodes taken with non-contact specular reflectometer over ten dust loading and cleaning cycles in an environmental chamber.

The initial clean specular reflection of the silver nanowire electrode mirror assembly was 91.3% at the start of the testing. Due to the higher transmission of the silver nanowire ink formulation, the initial specular reflectivity is higher than either of the other two electrode materials being tested. After sequentially loading the panel and activating the dust removal electrodes the specular reflection slowly decreased as with the other electrode materials. In each trial, after dust loading and activation of the electrodes, the specular reflection from the mirror increases. After the tenth trial, the

specular reflection after electrode activation was 78.4%.

Chapter 6

Optimization of Electrodes and Materials for Specular Reflection and Dust Clearance

6.1 Optimizing specular reflection

To create a dust removal device that will allow for cleaning operation and maintain a high level of reflectivity, the device will need to be optimized between the cleaning efficiency and the specular reflection. The electrodes will need to be optimized since they create the electric field that causes dust removal, and also block light and create diffuse reflection of solar radiation. Specular reflectivity can be increased by changing the percentage of the surface of the solar reflector that is covered by the electrodes, or by using a more optically transparent conducting material. Along with minimizing the optical area covered by the electrodes, the ratio of the width of the electrode to the spacing between electrodes correlates with specular reflection.

The values for optimization being reviewed are the electrode width and electrode spacing, and how these parameters contribute to specular reflection and dust removal performance. To optimize the overall specular reflection as the dust removal mirror would perform after repeated exposure to dust over several days, the overall specular reflection needs to be evaluated along with the dust removal performance normalized

against the initial reflection.

6.2 Optimization parameters space

The electrode geometry chosen to for this experiment was chosen by the constraints of fabrication technology, which in this case was photolithographic fabrication of electrodes, and performance based on previous modeling and experimental results. Fabrication of three phase electrodes using single-layer photolithography and chemical etching of chrome layered on borosilicate glass allows for only a single layer design, and no overlapping electrodes. A continuous three phase pattern can only be made by making a spiral design with this fabrication method. An image of the design is shown in figure 1-4. This method is not robust for scaling to larger sizes, since each phase of the electrode extends over the surface of the panel, creating more points of failure and increasing the resistance of the electrode.

While the spiral design is useful for laboratory testing due to the ease of making electrical connections to the three phase power supply, the design does not allow for dust to be directionally pushed down with a traveling electrostatic wave, but instead, pushes dust outward radially, which can lead to dust being pushed onto adjacent panels. Instead of creating a continuous phase for the entire surface, creating multiple connections and bridging over phases externally can be employed to create a three phase design.

With this design, two busbars are used to connect two separate phases to the electrodes on the surface, where the electrodes extend out from the bus bars at opposite sides of the design. Each of these phases have a single electrical connection

point. The connection of the third phase electrodes is connected to each electrode individually through a connection pad, which is larger than the electrode so that it allows for a manual connection to be made. These connections are made with a Mylar strip that has matching holes cut using a CNC laser cutter. The Mylar strip has an adhesive side which allows for a direct placement and seal over the connection points, and acts as a dielectric barrier between the overlapping electrodes. An image of the CAD design for this pattern is shown in figure 1.5.

This design has constraints in spacing due to the limited space that can be used to make the interconnections to each set of electrodes manually. The minimum spacing between each electrode set is determined by the size of the hole that can be reliably cut in the Mylar interconnection strip by the CNC laser cutting machine. For the Mylar material using an Epilog Zing laser cutter, the minimum spacing between holes is approximately 500 microns. Allowing spacing for a 1000 micron hole for electrical connection in the Mylar strip, the minimum electrode spacing that can be reliably connected and tested with this method is 300 microns. In addition to the limiting factors of fabrication, the specular reflection for closely spaced electrodes is greatly diminished as the ratio of electrode width to electrode spacing is increased and as the percentage of area covered by electrodes increases, as shown in table 6.1. For the maximum limits of testing electrode spacing, empirical studies showing decreased dust removal for electrodynamic screens with spacing at 1000 microns using a 1 kilovolt applied voltage were used to determine the upper bounds of electrode spacing.

The minimum electrode width was limited by the ability to reliably fabricate the electrodes without breaks. As the panels are fabricated with smaller electrode

widths, the fabrication process becomes more difficult. Misalignment of masks or dust particles present during the exposure of the photoplate can lead to broken electrode lines in the pattern. In addition to the difficulty of fabricating these panels, the finer electrodes are more susceptible to damage during the operation of the panel, if there is a presence of air bubbles in the vicinity of the electrode when it has been encapsulated. When a high voltage is applied to the electrodes, if there is an air bubble present it can cause arcing between adjacent electrodes and a failure of the panel.

Table 6.1: Table of electrode geometry studied in the optimization testing.

Panel Number	Electrode Width	Electrode Spacing	Ratio of width to spacing	Percent coverage of electrodes	Specular Reflection
1	50	500	10.00	9.09	84.7
2	50	800	16.00	5.88	87.9
3	100	300	3.00	25.00	67.8
4	200	700	3.50	22.22	78.3
5	300	400	1.33	42.86	57.5
6	300	300	2.00	33.33	69.2
7	300	900	3.00	25.00	73.5
8	500	500	1.00	50.00	62.6
9	500	800	1.60	38.46	68.9
10	600	400	0.67	60.00	53.6
11	800	300	0.38	72.73	48.4
12	25	800	32.00	3.03	91.5
13	5	800	160.00	0.62	93.0

As the electrode width decreases, the specular reflection increases, as shown in table 6.1. Along with the decreased electrode width, the ratio of width to spacing and percent coverage becomes correlated with high specular reflection. From the results shown in table 6.1 the panels with the highest specular reflection all have electrode widths smaller than 100 microns, ratios of electrode width to spacing greater than 1:10, and percentage coverage of electrodes less than 10 percent of the optical surface of the reflector. This becomes clear that for the best initial specular reflection, the electrodes should cover as small of a percentage of the reflector surface as possible, and the electrodes should be as narrow as allowable by the fabrication method.

The electrode geometries that were studied are shown in figure 6-1. In this figure, the horizontal axis represents the width of the electrodes tested, the vertical axis shows the inter-electrode spacing for each test panel. Each point on the graph shows a fabricated panel that was tested for performance and specular reflection. Although there were panels tested from several combinations of large and small spacing and varying electrode widths, more panels with smaller electrodes were tested since the initial specular reflection would be higher using the non-transparent chromium electrodes. Panels using transparent conducting materials would have different optical performance, and could be evaluated with different initial specular reflection readings for larger electrode widths and smaller spacings.

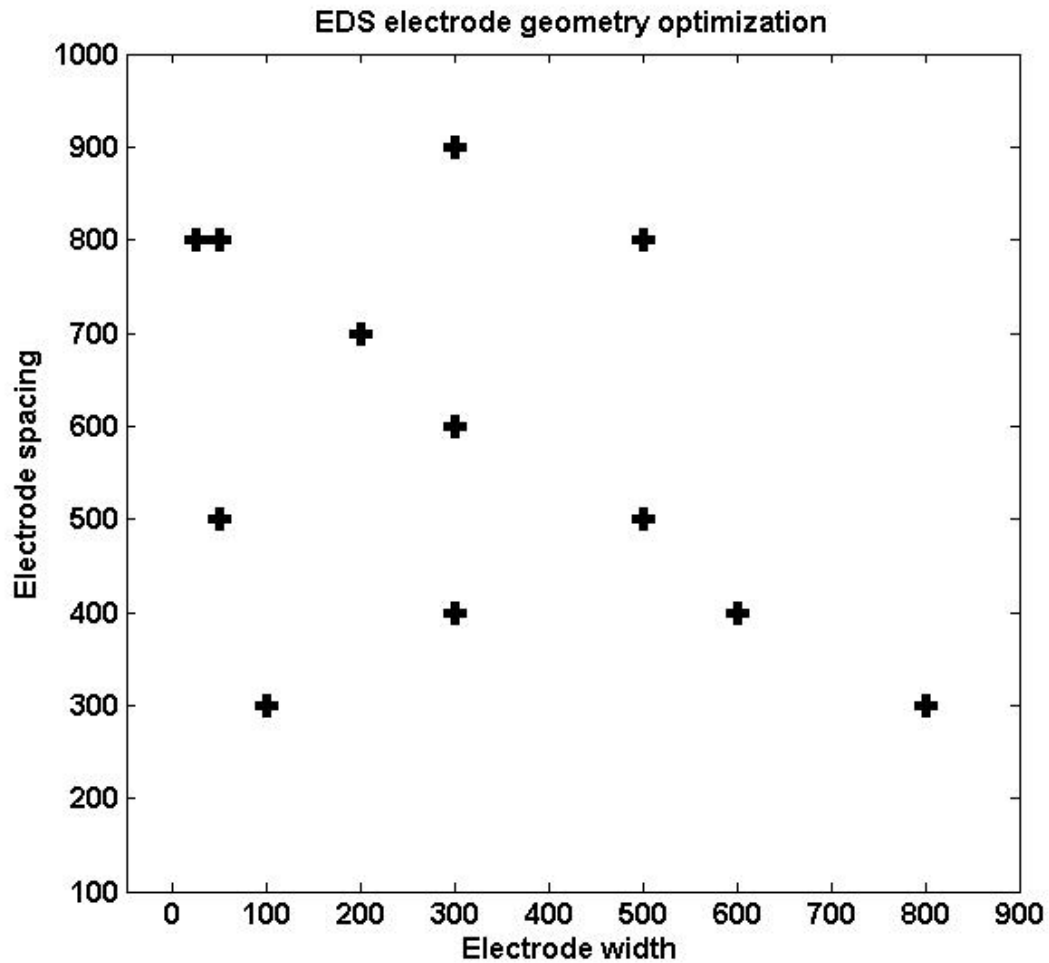


Figure 6-1: Plot of the optimization parameters. The electrodynamic screen parameters shown are the inter-electrode spacing on the y-axis, and the width of the electrodes on the x-axis. Each point on the plot represents a testing point in the study.

6.3 Specular reflection model using FRED ray tracing software

To evaluate the optical properties of the self-cleaning mirrors, an optical model was created using FRED Optical Engineering software. This software is a ray tracing program that allows optical models to be created in a CAD environment. FRED has

predefined optical materials, and also allows for custom optical materials based on laboratory measurements of optical index and attenuation. In this optimization model, the electrodes were being fabricated from chromium thin film coated photomasks, which were manufactured to have a low first surface reflection of approximately 60 percent.

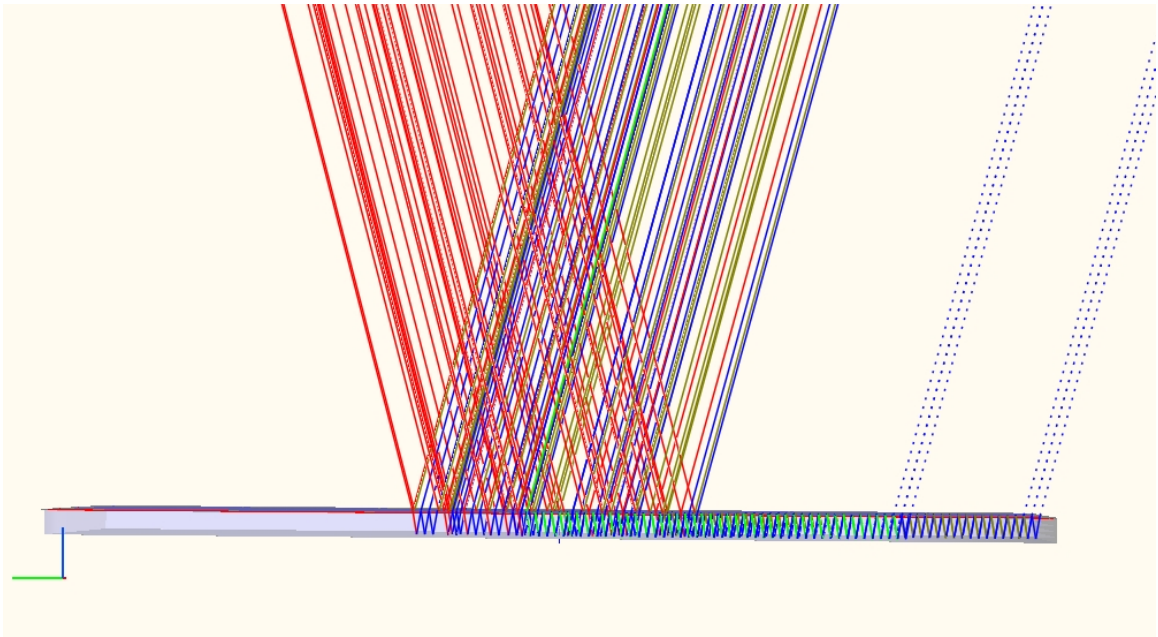


Figure 6-2: Image of the CAD model with ray tracing lines drawn from FRED Optical Engineering software, showing multiple reflections from the mirrored surface and embedded electrodes.

The software allows for a custom source to be used as a solar simulation source, and a specific target as a collector to analyze the reflected rays in the simulation. An example of a CAD model of an electrodynamic screen is shown in figure 6-2. The geometry of the electrodes is not easily viewed in the figure, as the dimensions are extremely small and would have to be greatly exaggerated from this view. Although this is not shown, the reflected rays that have been traced by the simulation can be

easily seen in this figure. The rays shown in red are the rays being emitted from the source in the simulations. After the simulated rays reach the optical surface and interact with a component, the color of the ray in the simulation is changed based on what part of the model it reflects or passes through.

In the CAD model, the first component the simulated rays will interact with will be a thin borosilicate glass that acts as the dielectric barrier layer shown in figure 1.2. For this component, the thin borosilicate glass layer has almost no absorption and a very small reflection coefficient, the values for these were taken from the values given by the glass manufacturer. After passing through the glass, the next medium the model interacts with is an optically clear adhesive, which is modeled as an optical cement in FRED. The next element that is modeled is the electrodes, which are made from low reflective chromium. The reflection coefficient and index of refraction are taken from the information provided by the photoplate manufacturer. An example of the modeled electrodes are also shown in figure 1.2. After interaction with the electrodes and optical adhesive layer, the rays will interact with a thicker borosilicate glass substrate and then a reflective surface, which are also shown in figure 1.2.

The reflections from each of these layers are displayed in the simulation as separate colors for each reflection. After the simulated rays pass through the layers of the model, they will reflect from the final mirrored surface and again go back through each layer of the model. In each layer the reflection of the ray will be noted by a change in color of the ray in the simulation environment. In some cases rays will be reflected multiple times in the glass substrate, reflecting from the back of the chrome electrodes back to the mirrored surface, as shown in the image of the simulation in

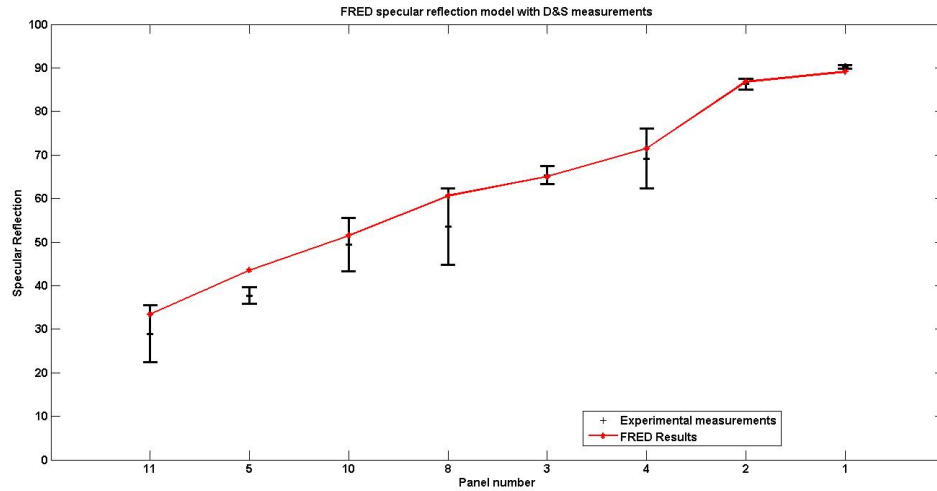


Figure 6-3: Plot of predicted specular reflection from the FRED ray tracing model is shown in the red line. The plot of the specular reflection measurements from the fabricated test panels is shown in the black points.

figure 6-2. This multiple reflection will greatly decrease the overall specular reflection of the self-cleaning mirror assembly, as the electrodes will completely block the rays multiple times, and will increase with the width of the electrode. For each electrode geometry in this study, the simulation was ran for the specific geometry and tested with the optical source in two cases, one where the electrodes were perpendicular to the horizontal, another with the electrodes parallel to the horizontal. In the case where the electrodes were perpendicular to the horizontal, the simulated rays would pass behind the electrodes and reflect multiple times from the mirror to the rear of the electrode. In the case where the electrodes were parallel to the horizontal, the electrodes would not cause multiple reflections from the rear of the electrode, and would have a greater specular reflection, especially in cases where the electrode width was larger.

6.4 Electrostatic force modeling

The electrostatic forces responsible for removing dust particles from the surface of an optical reflector are the Coulomb force, the dielectrophoretic force, and in some cases the gravitational force. The forces causing the dust particles to adhere to the surface of optical reflectors are the electrostatic image force, the Van der Waals force and gravitational force when surfaces are horizontal (Calle et al., 2009) (Horenstein et al., 2013b) (Horenstein et al., 2013a).

For the particles on the surface of the panel to be removed, the repulsive forces must be greater than the adhesive forces. The main repulsive force on the particles will be the Coulomb force, which is provided by the electric field that is created by the application of the three phase voltage on the electrodes. The Coulomb force for two particles interacting is shown in equation 6.1. For the Coulomb force that particles in the applied electric field, the particles will experience a force proportional to the applied electric field, as shown in equation 6.2. In this equation, q is the charge on the particle, and the electric field, E , is given by equation 6.3. For the electric field shown in equation 6.3, the magnitude of the field strength is determined by the applied voltage, V , and the distance between the two electrodes, g .

$$F_{Coulomb} = k_e \frac{q_1 q_2}{r^2} \quad (6.1)$$

$$F_{Coulomb} = q \hat{E}(x, y, z, t) \quad (6.2)$$

$$E = \frac{V}{g} \quad (6.3)$$

The field strength is given at the surface of the reflector, where the sand particles will experience the greatest adhesion forces. To overcome the adhesion forces, the applied Coulomb force, plus the gravitational force must be greater than the adhesive forces, as shown in equation 6.7. This field strength can be increased by increasing the applied three phase voltage to the electrodes, but will be limited to the breakdown voltage of the dielectric material in which the electrodes are embedded. In this case the material is borosilicate glass, which has a relative permittivity of 5 to 6 (Corning Willow, 2013). Since the field strength is also a function of the separation between the adjacent electrodes, increasing electrode spacing will decrease the dust removal force applied to the sand particles. From the results shown in table 6.1, the specular reflection will be decreased as the spacing between adjacent electrodes is decreased, creating the need for optimization of the spacing for both specular reflection and dust clearance.

$$F_{Gravity} = mgsin(\theta) \quad (6.4)$$

The gravitational forces acting on the particle will depend on the angle of the angle of the reflector, which in most cases would not be horizontal. The gravitational force is shown in equation 6.4, where m is the mass of the particle, g is acceleration due to gravity, and θ is the angle of inclination of the panel. When the panel inclined the forces due to gravity will act to cause the particles to fall from the surface.

The adhesive forces that a particle experiences are the electrostatic image force, shown in equation 6.5, where q is the charge of a particle on the surface, ϵ_1 is the permittivity of the particle, ϵ_2 is the permittivity of the medium in which the particle resides, and r is the distance between the referenced ground plane to the particle.

$$F_{Image} = \frac{q^2}{16\pi\epsilon_1\epsilon_2r^2} \quad (6.5)$$

The Van der Waals force acts as a strong repulsive force for small particles at a very close distance, and is shown in equation 6.6. In equation 6.6, A is the Hamaker Constant which is given as $5 \times 10^{-20}J$ for borosilicate glass, d_p as the diameter of the particle, and r as the distance from the particle to the surface.

$$F_{VanderWaals} = \frac{Ad_p}{12r^2} \quad (6.6)$$

The simplified model of forces acting on the particle can be summed to give a net force on the particle, as shown in equations 6.7 and 6.8. By summing the adhesive and repulsive forces a net sum can be shown that will either act to repel or attract the particle to the surface of the reflector.

$$\sum F = \sum F_{adhesive} - \sum F_{repulsive} \quad (6.7)$$

$$\sum F = F_{Coulomb} + F_{Gravity} - F_{Image} - F_{VanderWaals} \quad (6.8)$$

For the force analysis of the system, the force needed to remove a given particle from the surface of the panel is considered. When the particle is removed from the

surface of the reflector, the adhesive forces, namely the Van der Waals force decreases greatly, allowing the particle to be removed by the traveling wave motion of the applied electrostatic field. Because of this consideration, the magnitude of the forces normal to the surface of the reflector are evaluated.

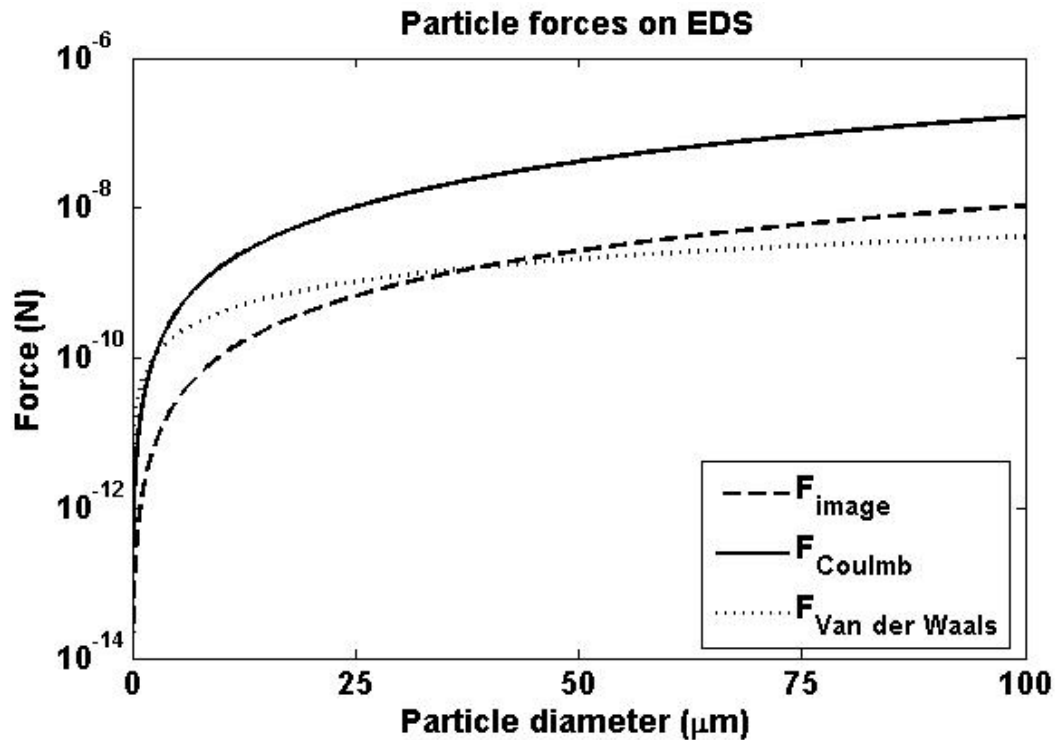


Figure 6-4: Plot of the forces acting on sand particles on an electrodynamic screen as a function of particle size. Force in newtons is shown on the y-axis, particle diameter in microns is shown on the x-axis. Forces plotted are the electrostatic image force as the dashed line, Coulomb force as the solid line, and Van der Waals force as the dotted line.

These forces acting on the particles are all a function of the diameter of the particle, which causes a difference in magnitude of force on a range of particle sizes. In testing and field studies, particle deposition has been shown to be from sub-micron to hundreds of microns. This broad range of particle sizes will cause smaller particles to adhere to the surface of the reflector even as larger particles are removed with the

same applied field strength. The electrostatic image force, Coulomb force, and Van der Waals force have been plotted for an electric field strength of $3MV/m^2$ and for particle size ranges from 10 nanometers to 100 micrometers in figure 6.4.

In the graph in figure 6.4, the electrostatic image force, Van der Waals force, and Coulomb force are all of small magnitude for particles less than a micron, the adhesive forces are larger than the repulsive Coulomb force. As the particle size increases, the Coulomb force increases at a faster rate than the Van der Waals force and the electrostatic image force, causing a net repulsive force acting on the larger sized particles. When the ratio of the adhesive and repulsive forces are plotted, it can show the net forces acting on the particle, as shown in the graph in figure 6.5. In this graph the ratio of the adhesive to repulsive forces is shown on the y-axis, and the particle diameter in microns is shown on the x-axis. The particle size ranges above a ratio of one will have a net repulsive force, where dust particles will be removed from the surface of the reflector.

As shown in figure 6.5, for particles less than two microns, the adhesion forces are still greater than the repulsive forces for this given electric field strength that was calculated. For the fine particles in this scenario to be removed, the electric field strength would need to be increased, or the adhesive forces would need to be decreased by lower surface energy of the reflector.

6.5 Optimization parameters and evaluation

To compare the effectiveness of dust removal as it relates to the overall increase in performance of a solar reflector, the dust removal efficiency alone can not be evaluated.

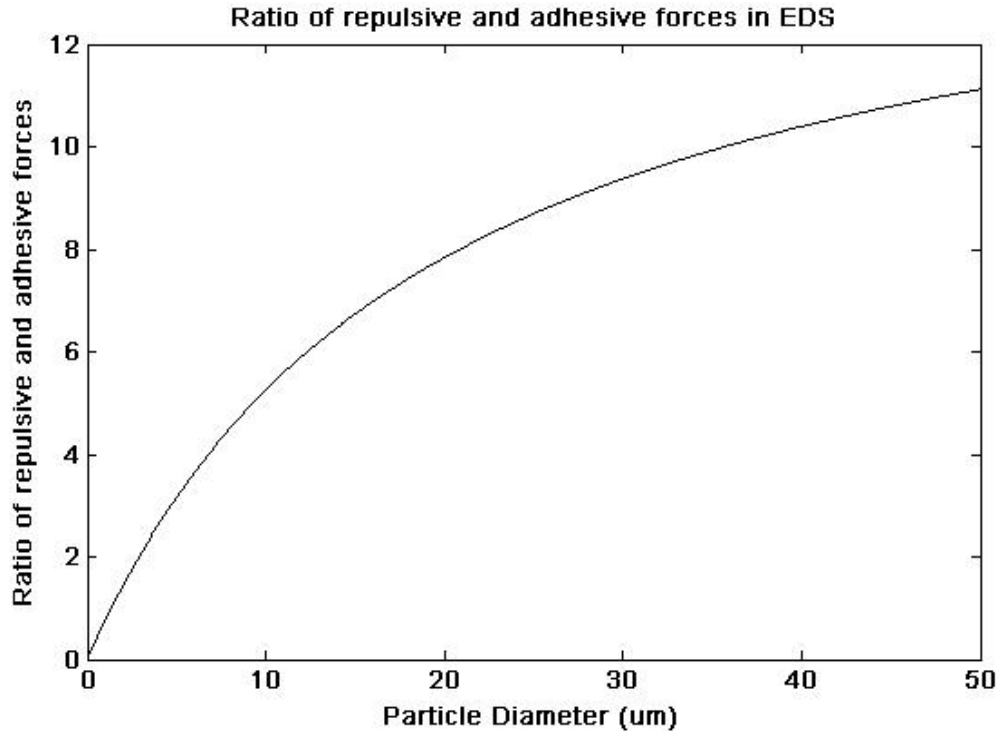


Figure 6-5: Plot of the ratio of adhesive and repulsive forces acting on sand particles on an electrodynamic screen as a function of particle size. The y-axis shows the ratio of forces, with a ratio over one being a net repulsive force. The x-axis shows the particle diameter in microns.

As shown in the previous sections of this chapter, the dust removal performance of the device will be increased as the electrode separation is decreased and the field strength is increased. The effect of decreasing electrode separation will cause specular reflectivity to greatly diminish, defeating the purpose of dust removal. The effect of clearance of dust and specular reflection will need to be studied independently to evaluate the performance of each selected electrode geometry.

To evaluate the performance of dust removal alone, an instrument was developed that takes multiple images over the surface of a solar reflector automatically using a motorized platform and digital microscope. This instrument called a Dust Deposition

Analyzer, DDA, feeds the images taken from the digital microscope into MATLAB, and using the MATLAB Image Processing Toolbox calculates the percentage of the image that is covered with dust particles. An image of the instrument is shown in figure 6-6, where the panel is placed directly onto the surface of the moving platform, and the digital microscope is in a fixed position above the sample. The motorized platform is controlled by a MATLAB program, and will take a digital image at every programmed point as it moves the sample under the microscope.

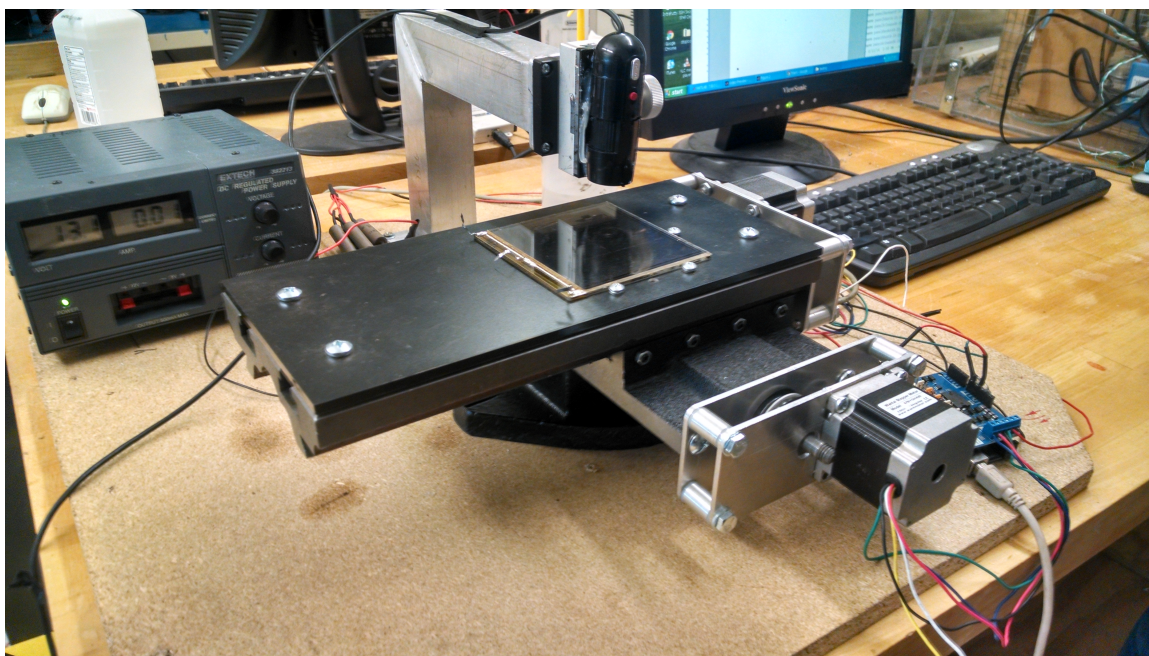


Figure 6-6: Image showing the Dust Deposition Analyzer, a device that scans the surface of a solar device and takes multiple images over the test surface. The instrument then uses MATLAB image processing toolbox to analyze the percentage of the surface area covered by dust particles.

After the instrument scans the surface of the test panel and collects the images, the program calculates the area of each image that is covered in dust particles, and then adds the entire area of the dust coverage for the entire panel. To effectively study

the dust removal using this technique, the panels were each imaged three times, once before dust was deposited onto the surface of the panel, again after the dust was deposited onto the surface of the panel, and once again after the dust removal electrodes were activated. At each point of the test, the specular reflection was also recorded. After imaging the panel at each trial with the DDA instrument, a surface plot of dust accumulation on the test panel was plotted, showing the change in dust after loading and after cleaning. The graph in figure 6.7 shows the surface plot, where a higher point in the z-axis shows a concentration of dust at that point in the x-y plane or surface of the panel.

The first surface plot in figure 6.7 shows the concentration of dust during the initial scan, where the panel was clean. The second surface plot shows the dust after deposition, and the final plot shows the dust after the dust removal electrodes have been activated. Using this data collected from the DDA, the percentage of dust clearance for each panel test was calculated by determining the total dust area removed after the activation of the panel. The percent clearance for each panel is shown in the third column of table 6.2. As with all of these panels, the percentage clearance was very high, and most of the dust deposited on the surface was removed. This is due to the selection of panel geometries being studied was limited to designs that would be able to remove dust effectively.

After the panels were tested using the DDA and the percent clearance for each panel was determined, the specular reflection for each panel was considered. Column two of table 6.2 shows the initial specular reflection of each panel, before dust was deposited on the surface. By taking this value into consideration along with the

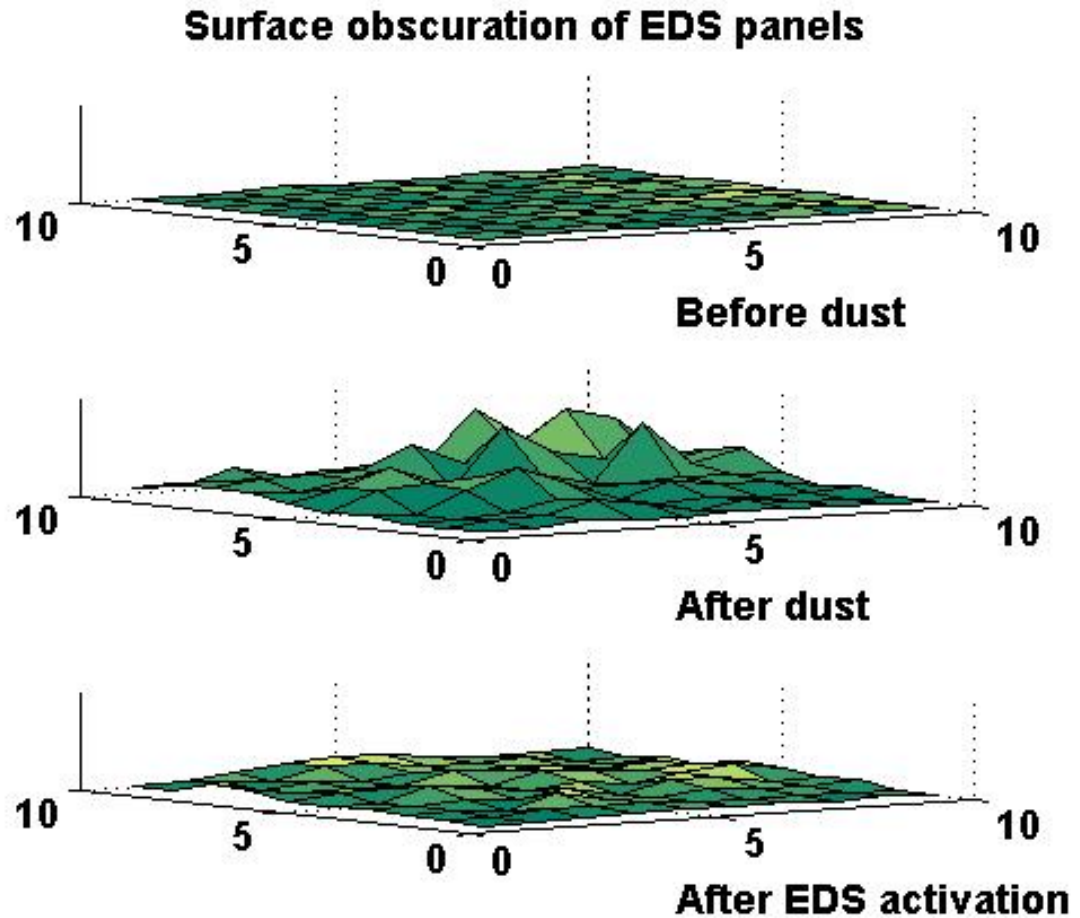


Figure 6-7: Images showing the clearance from a panel, using a dust particle imaging system to scan the surface and determine dust removal. The first image shows before dust deposition, the second image is after dust deposition, and the third is after EDS activation.

dust removal performance, a better concept of effective panel cleaning can be used. Equation 6.9 shows the product of the initial specular reflection and the percent clearance of the panel can be used as a clearance factor for each panel.

$$CF = R_{specular} \times Clearance \quad (6.9)$$

By taking the clearance factor the panel's initial specular reflection and overall

dust removal performance is considered, and the panels can be evaluated by this method. The fourth column in table 6.2 shows the clearance factor, as defined by equation 6.9. By using a metric of maintaining a 90 percent specular reflection and 90 percent dust removal efficiency as an effective clearance factor, it can be shown that several of these designs meet this goal using chrome electrodes. The graph in figure 6-8 shows the tested panels by number on the x-axis, and on the y-axis the panels clearance factor. The line plotted across the graph shows the level of 90 percent clearance factor.

Table 6.2: Table of measured specular reflection values, percent clearance, and the adjusted clearance factor.

Panel	$R_{spec}(\%)$	Clearance (%)	$R_{spec} * Clearance$
1	84.7	97.61	82.68
2	87.9	96.56	84.88
3	78.3	97.44	76.30
4	64.0	97.05	62.11
5	69.2	97.46	67.44
6	73.5	98.09	72.10
7	62.6	97.53	61.05
8	68.9	96.46	66.46
9	53.6	98.03	52.54
10	48.4	97.23	47.06
11	90.7	94.89	86.06

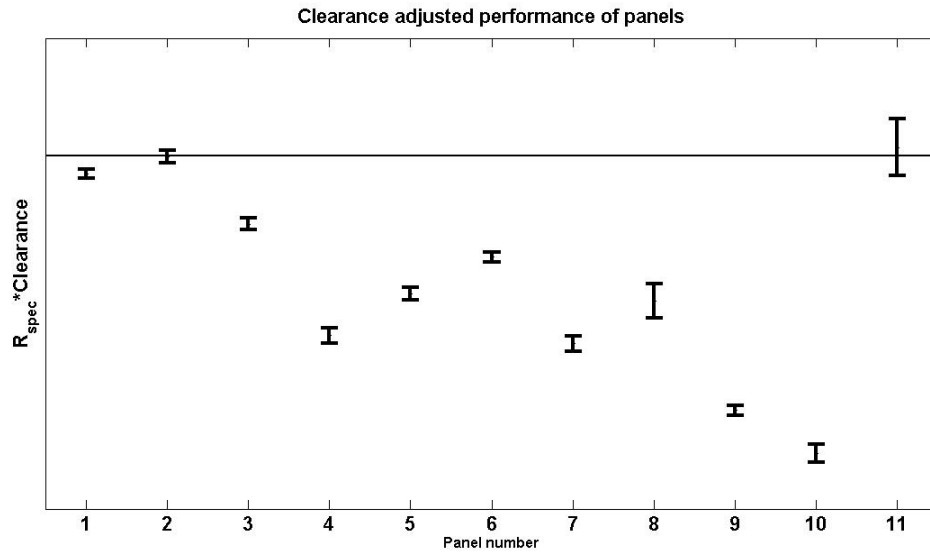


Figure 6-8: Plot showing the results of the clearance factor, which is a function of the initial specular reflection and the percent clearance of the panel. The line shows a 90 percent value of clearance and specular reflection.

6.6 Laboratory Testing of Dust Removal Mirrors

Test panels were constructed using various methods of fabrication and mounted to 3M 1100 series high specular reflection mirror film. The electrode materials evaluated for this work were non-transparent chrome electrodes patterned by photolithography and PEDOT:PSS conducting polymer ink, fabricated by traditional screen printing techniques. While chrome electrodes are good for producing a widely varied electrode geometry using lithography and have excellent electrical properties, they are still a non-transparent metal material, and will have significantly lower specular reflection because of this. PEDOT:PSS does have favorable electrical properties, but requires a fabricated screen to print the material, which makes electrode geometry more static. After patterning the electrodes, a protective dielectric layer was deposited onto the

panels via Mayer rod method. The material used was a 50 micron acrylic film. After the panels were fabricated, they were tested in an environmentally controlled chamber for specular reflection restoration. To avoid contamination of the testing procedure, a non-contact specular reflectometer was developed, which has a 15 degree angle of incidence, a 1.4 degree acceptance angle, and a 655 nanometer collimated LED source. The panels were tested by depositing test sand onto a panel from a sieve with vibration motors, while continuously monitoring specular reflection. After the initial deposition of dust, the panels were activated for one minute by a power supply that supplies a three-phase, 1kV, 5Hz, square wave voltage to the electrodes embedded onto the glass front surface of the mirror module. Specular reflection measurements were recorded before each dust deposition, after dust deposition, and again after the EDS module had been active for one minute.

Ten trials were completed consecutively without any additional cleaning between trials, and the environment was kept at approximately 22.5 degrees Celsius and 20% relative humidity. The performance of a PEDOT:PSS electrode panel is shown in figure 6-9, where the specular reflection measurements are shown by initial measurements in black, after dust loading in red, and after clearing in blue. For chrome electrodes, the dust clearing performance shows the same trends, with gradually decreasing specular reflection after repeated consecutive trials. The procedure for chrome electrode testing was identical, and a graph of the specular reflection is shown in figure 6-10.

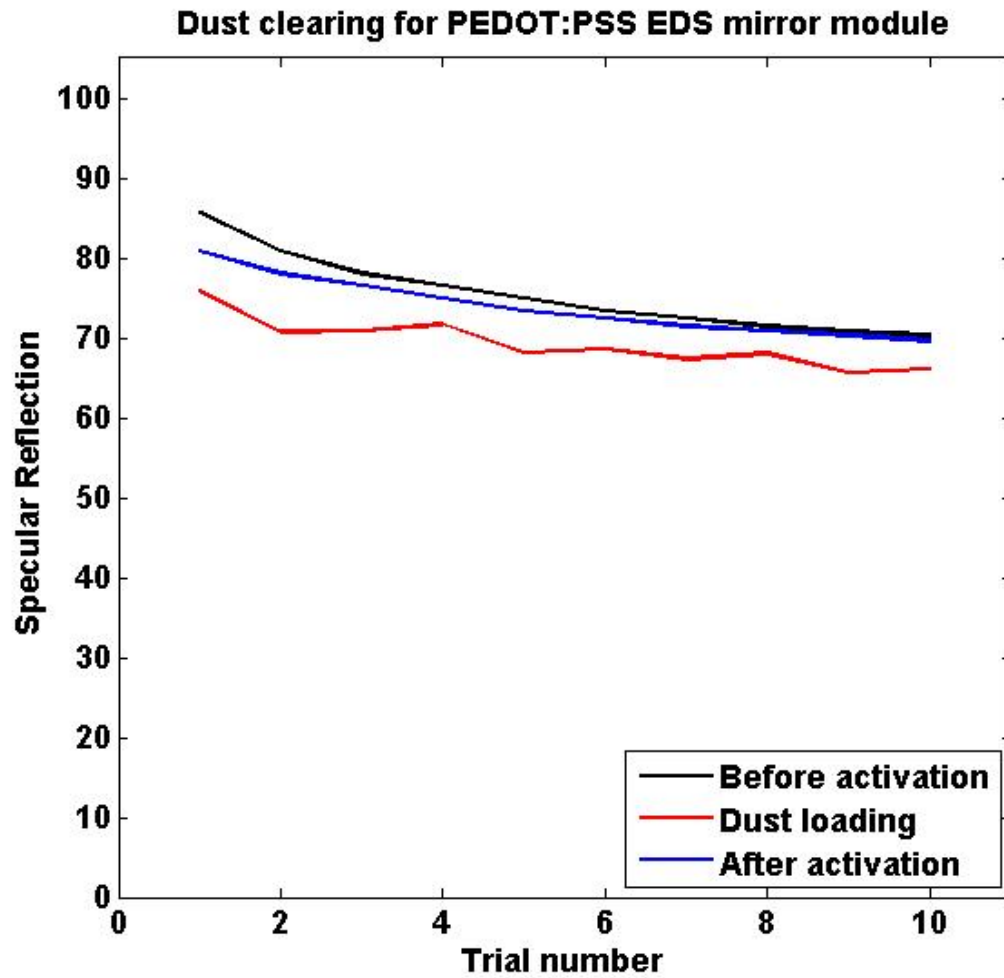


Figure 6-9: Laboratory testing for dust removal mirror module with PEDOT:PSS electrode materials.

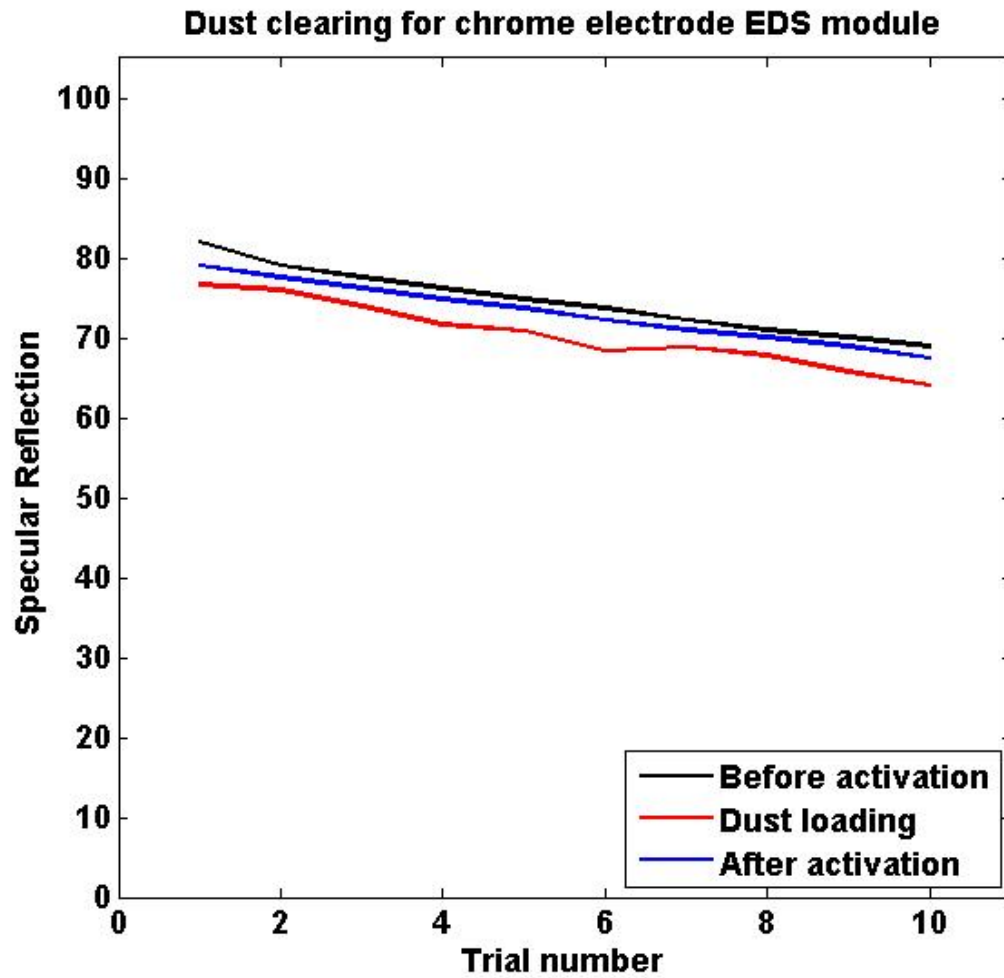


Figure 6-10: Laboratory testing for dust removal mirror module with chrome electrode materials.

Chapter 7

Development of a Three Phase Low Frequency Power Supply

7.1 Previously designed power supplies

Previously designed three phase, high voltage power supplies were designed to work at 1kV for dust removal processes. At this voltage the electrode geometry is generally constrained to a small spacing, which can decrease the specular reflection. If the electrode distance is increased, the field strength will decrease and cause a decrease in dust removal performance. Allowing a variation of voltage, up to and over 2kV will allow for a larger set of electrode geometries to be studied, and add more flexibility into future designs. The previously designed power supply was used for greater flexibility in varying the frequency and type of waveform, so that the concepts of frequency and type of waveform could be studied (Biris et al., 2004) (Mazumder et al., 2007).

The power supply design consisted of a three phase switching transistor network, which is used to switch a DC high voltage that is provided by a DC-DC high voltage converter from EMCO Corporation. The switching network is driven by a driver integrated circuit that is limited to 1.2 kilovolt maximum. The three-phase waveform is controlled by a Texas Instruments EZ2400 microcontroller module, which has RF communication capability. The input to the system is controlled through push

buttons connected to GPIO pins on the microcontroller. LED displays were used to show current frequency output, and were connected to shift bet registers from the microcontroller. An image of this power supply is shown in figure 7-1.

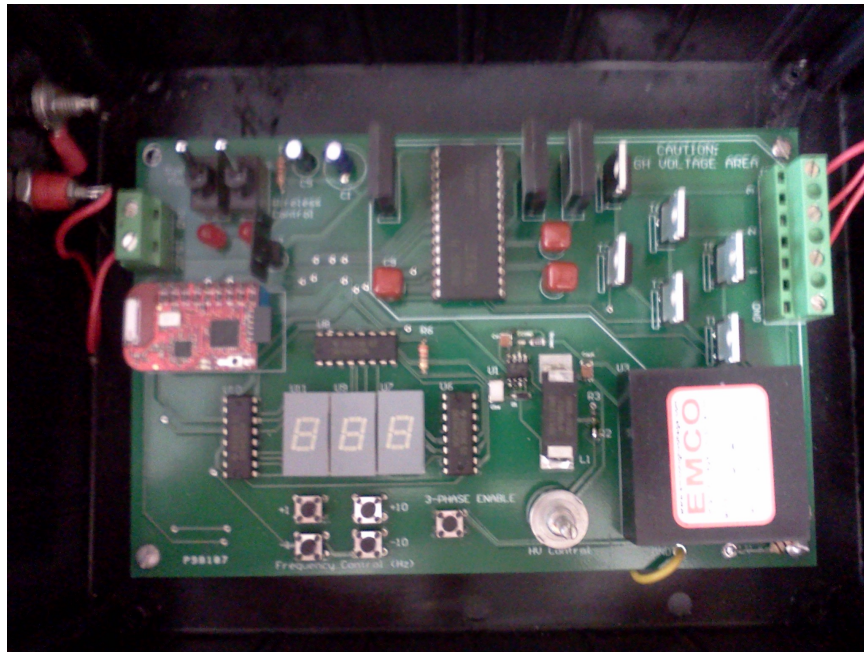


Figure 7-1: Image of a second generation power supply design.

7.1.1 Challenges encountered with old design

This design for the power supply was functional, but prone to failure in extended testing. While conducting extended testing on panels, several power of this generation power supplies would fail. After troubleshooting the dead supplies, the transistor driver was the cause of failure in most cases.

The failure of a power supply during panel testing can sometimes go unnoticed or recorded as an experiment where the panel experienced failure, or some other

Table 7.1: Table of specular reflection values for trial with failed power supply

Intial Specular Reflection	After Dust Deposition	EDS Activation
88.7	86.7	86.8
86.8	85.1	85.1
85.1	81	80.5
80.5	78.8	79.5
79.5	77	77.7
77.7	72.4	74.6
74.6	73.7	74
74	72.6	73.3
73.3	71	72
72	69.6	70.7

cause. This usually requires several rounds of troubleshooting, and can cause data to be skewed. An example of a failed power supply is shown in 7.1, where the power supply driver failed and one phase of the supply was not able to output the correct voltage. When this occurs the performance is diminished, and the specular reflection restoration is very minimal, leading to considerable dust accumulation.

7.1.2 Limitations with 1 kV design

With the failures that periodically occur, as shown in table 7.1, the components used in the previously designed supply do not make a suitable power supply for continued lab and field testing. Premature failure of three phase power supplies in testing leads to poor results in the performance of the panels, so the design for the supply needs to be more robust.

In addition to the premature failures of the high voltage components, the power supply design was limited to operation at approximately 1 kilovolt. As shown in the

previous chapters, the operation of the power supply at higher voltages can increase the effectiveness of dust removal, and allow for larger separation of electrodes, giving a higher specular reflection for dust removal mirrors. The ability to control the three phase output voltage in a range from 1 kilovolt to 2 kilovolts will have an impact on the ability to study the dust removal performance of many different panel designs, and increase the efficiency of the dust removal.

7.2 Simplified 2 kV power supply design

To overcome some of the limitations of the previous three phase power supply, a new supply was designed to allow for a higher voltage, with operation up to 2 kilovolts. Along with operating at a higher three phase output voltage, the supply needed to be more robust. The components needed to create a three phase high voltage supply are a three-phase waveform generator and a DC-DC high voltage converter. With the previous design, an EMCO corp GP12 DC-DC high voltage converter was used to create the high voltage output. To create a high voltage waveform at 2kV, an EMCO corporation GP30 model was used, which is capable of an output voltage of 3kV at 1mW of power. To eliminate failures caused by the burnout of the three-phase high voltage driver IC, this part was completely eliminated from the simplified design. The elimination of this driver IC and the switching network requires that three EMCO GP30 DC-DC converters are used, and the output of these acts as the floating output voltage for the dust removal panel.

Table 7.2: Rise and fall times for 2 kV waveform at 5 Hz.

Input Voltage	Output Voltage	Rise time	Fall time
5V	750V	3ms	17ms
6V	930V	4ms	17ms
7V	1100V	4ms	16ms
8V	1290V	3ms	15ms
9V	1500V	3ms	14ms
10V	1690V	3ms	13ms
11V	1860V	3ms	12ms
12V	2000V	4ms	12ms

By connecting the output from the EMCO directly to the panel, the floating voltage applied to the panels does not directly switch to ground, and the voltage decays very slowly. To overcome this slow decay time, a resistor network was added to the output of the DC-DC converter to increase the time constant of the voltage decay. Table 7.2 shows the rise and fall time of at 5Hz waveform at the output of the EMCO DC-DC converter with a $1M\Omega$ load resistor to decrease the fall time of the waveform. The waveform has a 12ms fall time at 2kV output, which would make the fall time approximately 6 percent of the period of the three phase waveform.

The three phase waveform was generated by a microcontroller, and each of the output GPIO pins were connected to a quad half h-bridge driver IC, Texas Instruments model SN754410, which would supply the input voltage to the EMCO DC-DC high voltage converter. This method of driving the DC-DC converters eliminated the need for the high voltage switching network and only relies on the DC-DC converter for the high voltage switching, making the system less likely to fail due to breakdown of high voltage components.

Table 7.3: Table showing the results of a trial with the 2kV supply applied after 10 trials with a 1kV applied three-phase voltage. The final trial shows a large increase in specular reflection after applying the 2kV three phase voltage.

Initial Specular Reflection	Loaded Specular Reflection	Specular Reflection After Activation	Applied Voltage
88.6	86.6	86.7	1kV
86.7	84.2	85.6	1kV
85.6	83.3	85.4	1kV
85.4	81.9	85.2	1kV
85.2	81.9	85.0	1kV
85.0	81.4	85.0	1kV
85.0	81.4	84.6	1kV
84.6	83.9	84.9	1kV
84.9	81.7	84.4	1kV
84.4	83.9	84.6	1kV
84.6	82.2	86.0	2kV

The performance of the 2kV three phase supply has the ability to consistently provide a 2kV three phase waveform to the dust removal mirrors. The performance of the 2kV supply is shown by using the 2kV supply after ten consecutive trials with a 1kV supply. After the dust loading and removal trials were completed with the 1kV supply, the 2kV supply was connected to the dust removal mirror and the 2kV supply was activated. The results from the trial are shown in table 7.3, where the final trial is for the 2kV supply.

In this trial, the 2kV supply is activated after 10 consecutive trials at the lower voltage, and the specular reflection is restored to within two percent of the original specular reflection. Applying the higher voltage will create a stronger electric field and

remove particles that would not have been removed with the electric field magnitude that was created by the 1kV power supply.

Chapter 8

Conclusion

This work has shown that solar reflectors with embedded dust removal electrodes can act as an effective method of removing dust from solar modules and restoring reflected optical power to collectors. Through the optimization and implementation of these devices, solar modules can achieve greater efficiency by keeping dust deposition to a minimal level in environments with high levels of dust accumulation. Modeling the optical system of embedded electrodes in a glass substrate has shown this method to be an optically and electrostatically viable solution for dust removal, with optical losses of less than one percent due to the inclusion of the electrodes in a solar reflector module. Fabrication and testing of these modeled devices has shown dust removal efficiency above ninety-five percent in laboratory simulated tests. Through the study of specific sand types and environmental conditions, operating parameters have been determined to show this method can work in a variety of settings, with a range of sand types. Although high voltage supplies are needed to generate the electrostatic field to remove dust, the power supply design is low power, using less than a watt to drive a square meter of dust removal. The power supply can also be integrated into a control system or existing power conditioning hardware, allowing for lower cost and greater control of dust removal. The small amount of power used for this device

would be greatly offset by the amount of power saved by allowing more transmission of light to solar surfaces.

8.1 Future Work

Pilot scale deployment of dust removal modules should be tested to determine the longevity and effectiveness of dust removal modules in environmental conditions. The effects of long term solar irradiation and weathering will need to be developed to observe lasting effects of dust removal in solar modules. Short term testing does show the effect of higher specular reflection after electrostatic cleaning, but long term deposition and reliability will need to be established and optimized for commercial development. Pilot scale testing must be done to establish effectiveness of materials and methods currently tested.

References

- Al-Hasan, A. Y. (1998). A new correlation for direct beam solar radiation received by photovoltaic panel with sand dust accumulated on its surface. *Solar Energy*, 63(5):323–333.
- Biris, A. S., Saini, D., Srirama, P. K., Mazumder, M. K., Sims, R. a., Calle, C. I., and Buhler, C. R. (2004). Electrodynamic removal of contaminant particles and its applications. *Conference Record of the 2004 IEEE Industry Applications Conference 2004 39th IAS Annual Meeting*, 2(C):1283–1286.
- Calle, C. I., Buhler, C. R., McFall, J. L., and Snyder, S. J. (2009). Particle removal by electrostatic and dielectrophoretic forces for dust control during lunar exploration missions. *Journal of Electrostatics*, 67(2-3):89–92.
- Chaudhry, A. M., Fairbanks, D. H., and Caldwell, A. (2015). Determinants of Water Sales During Droughts: Evidence from Rice Farm-Level Data in California. Technical report.
- Corning Willow (2013). Corning Display Technologies — Corning Willow Glass. Technical Report cm.
- Goossens, D. and Offer, Z. (1990). A wind tunnel simulation and field verification of desert dust deposition (Avdat Experimental Station, Negev Desert). *Sedimentology*, 37:7–22.
- Goossens, D. and Offer, Z. (1995). Comparisons of day-time and night-time dust accumulation in a desert region. *Journal of Arid Environments*, pages 253–281.
- Green, M. and Emery, K. (2012). Solar cell efficiency tables (version 39). *Progress in Photovoltaics: Research and Applications*, 20(1):12–20.
- Gregory, G. G. and Koshel, R. J. (2006). Modeling the operating conditions of solar concentrator systems. In Gombert, A., editor, *Proceedings of SPIE 6197, Photonics for Solar Energy Systems*, pages 61970J–61970J–11.
- Ho, C. Software and codes for analysis of concentrating solar power technologies. *Sandia Report SAND2008-8053*, (Available from http://infoserve.sandia.gov/sand_doc/2008/088053.pdf).

- Horenstein, M. N., Mazumder, M., and Sumner, R. C. (2013a). Predicting particle trajectories on an electrodynamic screen Theory and experiment. *Journal of Electrostatics*, 71(3):185–188.
- Horenstein, M. N., Mazumder, M. K., Sumner, R. C., Stark, J., Abuhamed, T., and Boxman, R. (2013b). Modeling of Trajectories in an Electrodynamic Screen for Obtaining Maximum Particle Removal Efficiency. *IEEE Transactions on Industry Applications*, 49(2):707–713.
- Jones, T. B. (2003). Basic Theory of Dielectrophoresis and Electrorotation. *IEEE Engineering in Medicine and Biology Magazine*, 22(6):33–42.
- Mathews, J. a. and Tan, H. (2013). The transformation of the electric power sector in China. *Energy Policy*, 52:170–180.
- Mazumder, M., Biris, A., Trigwell, S., Sims, R. A., Calle, C. I., and Buhler, C. R. (2003). Solar panel obscuration in the dusty atmosphere of Mars. *Proceedings of the ESA-IEEE Joint Meeting on Electrostatics 2003*, (2):208–218.
- Mazumder, M., Horenstein, M. N., Stark, J. W., Girouard, P., Sumner, R., Henderson, B., Sadler, O., Hidetaka, I., Biris, A. S., and Sharma, R. (2013). Characterization of Electrodynamic Screen Performance for Dust Removal from Solar Panels and Solar Hydrogen Generators. *IEEE Transactions on Industry Applications*, 49(4):1793–1800.
- Mazumder, M., Sharma, R., Biris, A. S., Zhang, J., Calle, C., and Zahn, M. (2007). Self-cleaning transparent dust shields for protecting solar panels and other devices. *Particulate Science and Technology*, 25(1):5–20.
- Mazumder, M., Yellowhair, J., Stark, J., Heiling, C., Hudelson, J., Hao, F., Gibson, H., and Horenstein, M. (2014). Optical and adhesive properties of dust deposits on solar mirrors and their effects on specular reflectivity and electrodynamic cleaning for mitigating energy-yield loss. In *Proceedings of SPIE 6915*, volume 691523, page 91750K.
- Moore, A. D. (1973). *Electrostatics and Its Applications*. John Wiley & Sons, Ltd.
- Morton, O. (2006). A New Day Dawning. *Nature*, 443(September):19–23.
- Niknia, I., Yaghoubi, M., and Hessami, R. (2012). A novel experimental method to find dust deposition effect on the performance of parabolic trough solar collectors. *International Journal of Environmental Studies*, 69(2):233–252.
- Offer, Z. Y. and Goossens, D. (2001). Ten years of aeolian dust dynamics in a desert region (Negev desert, Israel): analysis of airborne dust concentration, dust accumulation and the high-magnitude dust events. *Journal of Arid Environments*, 47(2):211–249.

- Pettit, R. and Freese, J. (1980). Wavelength dependent scattering caused by dust accumulation on solar mirrors. *Solar Energy Materials*, 3(1-2):1–20.
- Qasem, H., Betts, T. R., Müllejans, H., AlBusairi, H., and Gottschalg, R. (2014). Dust-induced shading on photovoltaic modules. *Progress in Photovoltaics: Research and Applications*, 22(2):218–226.
- Sarver, T., Al-Qaraghuli, A., and Kazmerski, L. L. (2013). A comprehensive review of the impact of dust on the use of solar energy: History, investigations, results, literature, and mitigation approaches. *Renewable and Sustainable Energy Reviews*, 22:698–733.
- Sharma, R., Trigwell, S., Biris, A. S., Sims, R. A., and Mazumder, M. K. (2003). Effect of ambient relative humidity and surface modification on the charge decay properties of polymer powders in powder coating. *IEEE Transactions on Industry Applications*, 39(1):87–95.
- Sims, R. A., Biris, A. S., Wilson, J. D., Yurteri, C. U., Mazumder, M. K., Calle, C. I., and Buhler, C. R. (2003). Development of a transparent self-cleaning dust shield for solar panels. In *J.M. Crowley (ed.) Proceedings of the ESA-IEEE Joint Meeting on Electrostatics*. Laplacian Press., (1):814–821.
- Solomon, S., Plattner, G.-K., Knutti, R., and Friedlingstein, P. (2009). Irreversible climate change due to carbon dioxide emissions. *Proceedings of the National Academy of Sciences of the United States of America*, 106(6):1704–9.
- Wendelin, T. In Thornbloom, M. D. and Jones, S. A., editors, *Solar Engineering 2003: Presented at the 2003 International Solar Energy Conference (pp. 253-260)* New York: American Society of Mechanical Engineers.

CURRICULUM VITAE

Jeremy Stark

www.jeremystark.com

WORK

Electronics Engineer
MagCanica, 2015-Present

Research Assistant
Boston University Applied Electromagnetics Lab 2009-2015

Research Assistant
UALR Particulate Materials Science and Engineering Research Lab, 2008-2009

EDUCATION

Boston University
Electrical Engineering (Ph.D.), May 2016
Electrical Engineering (M.S.), May 2012

University of Arkansas at Little Rock
Systems Engineering (B.S.), May 2009
Physics (B.S.), May 2009

TEACHING EXPERIENCE

Control Systems, EC402
Boston University
Graduate Teaching Fellowship, Spring 2015

Senior Capstone Design, ME414
Boston University
Graduate Teaching Fellowship, Spring 2012

Introduction to Electronics, EC4010
Boston University
Graduate Teaching Fellowship, 2010

PAPERS AND PRESENTATIONS

- “ Development of Transparent Electrodynamic Screens on Ultrathin Flexible Glass Film Substrates for Retrofitting Solar Panels and Mirrors for Self-Cleaning

Function”, MRS Advances, M.K. Mazumder, J.W. Stark, C. Heiling, M. Liu, A. Bernard, M. N. Horenstein, S. Garner, H.Y. Lin.

- “Environmental Degradation of the Optical Surface of PV Modules and Solar Mirrors by Soiling and High RH and Mitigation Methods for Minimizing Energy Yield Losses”, 2015 IEEE 42nd Photovoltaic Specialist Conference (PVSC), New Orleans, LA, M.K. Mazumder, M.N. Horenstein, C. Heiling, J. W. Stark, A. Sayyah, J. Yellowhair, A. Raychowdhury.
- “Optical Modeling of Reflectivity Loss Caused by Dust Deposition on CSP Mirrors and Restoration of Energy Yield by Electrodynamic Dust Removal”, ASME 2014 Conference on Energy Sustainability and Fuel Cell Science, Boston, MA, Jeremy Stark, Julius Yellowhair, John N. Hudelson, Mark Horenstein, and Malay Mazumder
- “Development and Evaluation of Prototype Transparent Electrodynamic Screen (EDS) Integrated Solar Collectors for Automated Dust Removal”, ASME 2014 Conference on Energy Sustainability and Fuel Cell Science, Boston, MA, John N. Hudelson, Jeremy Stark, Fang Hao, Zhongkai Xu, Hannah Gibson, Mark N. Horenstein, and Malay Mazumder
- “Optimization of Electrodynamic Screens for Efficient Removal of Dust Particles”, ASME 2014 Conference on Energy Sustainability and Fuel Cell Science, Boston, MA, Arash Sayyah, Jeremy W. Stark, John N. Hudelson, Mark N. Horenstein, and Malay K. Mazumder
- “Self-Cleaning Solar Mirrors Using Electrodynamic Dust Shield: Prospects and Progress”, ASME 2014 Conference on Energy Sustainability and Fuel Cell Science, Boston, MA, Malay K. Mazumder, Mark N. Horenstein, Nitin Joglekar, Jeremy W. Stark, John N. Hudelson, Arash Sayyah, Julius Yellowhair, and Adam Botts
- “Electrodynamic removal of dust from solar mirrors and its applications in concentrated solar power (CSP) plants”, Industry Applications Society Annual Meeting, 2014 IEEE, Vancouver, BC, M. Mazumder, M. Horenstein, J. Stark, J.N. Hudelson, A. Sayyah, C. Heiling, J. Yellowhair.
- “Optical and adhesive properties of dust deposits on solar mirrors and their effects on specular reflectivity and electrodynamic cleaning for mitigating energy-yield loss”, SPIE Proceedings 2014, Malay Mazumder, Julius Yellowhair, Jeremy Stark, Calvin Heiling, John Hudelson, Fang Hao, Hannah Gibson, Mark Horenstein.
- “Optimization of Electro-optic Systems for Self Cleaning Photovoltaic Panels and Concentrated Solar Reflectors”, Presentation at ESA 2009 Annual Meeting on Electrostatics

- “Development of Self-Cleaning Solar Collectors for Minimizing Energy Yield Loss Caused by Dust Deposition”, ASME 2013 Conference on Energy Sustainability, Minneapolis, MN.
- “Development of Self-Cleaning Solar Mirrors Utilizing Transparent Electrodynamic Screens”, Presentation at ESA 2009 Annual Meeting on Electrostatics
- “Characterization of Electrodynamic Screen Performance for Dust Removal from Solar Panels and Solar Hydrogen Generators”, IEEE Transactions on Industry Applications 2013, Malay Mazumder, Mark Horenstein, Jeremy Stark, Peter Girouard
- “Modeling of Trajectories in an Electrodynamic Screen for Obtaining Maximum Particle Removal Efficiency”, IEEE Transactions on Industry Applications 2013, Mark Horenstein, Malay Mazumder, Rob Sumner, Jeremy Stark, Tareq Abuhamed, Ray Boxman
- “Developments in Surface Contamination and Cleaning: Particle Deposition, Control, and Removal”, Chapter contributions, Electrostatic Removal of Particles and its Applications to Self-Cleaning Solar Panels and Solar Concentrators
- “Mathematical Simulation Study of Digital Signal Processing of the ESPART Analyzer for the Nanoparticle Size Range”, ESA 2009 Annual Meeting on Electrostatics, Jeremy Stark, Jing Zhang, Rajesh Sharma, Malay Mazumder
- “Measurement of Electrostatic Charge and Aerodynamic Diameter of Sub-Micron Particles by the ESPART Analyzer”, ESA 2008 Annual Meeting on Electrostatics, Jeremy Stark, Jing Zhang, Rajesh Sharma, Al Adams, Malay Mazumder
- “Non-contact Measurements of Size and Charge Distributions of Submicron Particles using an ESPART Analyzer”, IEEE Transactions on Industry Applications 2007, Praveen Srirama, Jeremy Stark, Jing Zhang, Malay Mazumder